A further look at Archard’s Equation to extract additional information from the material loss ~ load curve

by

Abu Hasnat Mohammad Azadur Rahman

A thesis submitted in partial fulfillment of the requirements for the degree of

Master of Science

In

Materials Engineering

Department of Chemical and Materials Engineering
University of Alberta

© Abu Hasnat Mohammad Azadur Rahman, 2018

Abstract

Archard’s wear equation has been widely used in industry for preliminary selection of materials mainly based on hardness. According to Archard’s equation, the material wear rate is linearly proportional to the normal force. However, the wear rate or material volume loss per unit sliding distance is usually not linear with the normal force. The non-linear relationship should result from variations in the resistance of a material to wear due to changes in the mechanical behavior of materials such as strain-hardening capability. In this study, we performed sliding wear tests to determine and analyze the material loss – normal load curves of three alloys, Al5182 (FCC), AZ 31 alloy (HCP) and the high strength low alloy (HSLA) steel (BCC). The volume loss ~ normal load curves did not appear as straight lines. An attempt was made to understand this phenomenon and extract additional information from the non-linear volume loss ~ normal load relationship.

Preface

The materials presented in the current thesis are parts of a research supervised by Dr. Dongyang Li. Samples for this research presented in chapter 3 and the tensile test data presented in chapter 4 were provided by Dr. Daolun Chen, Department of Mechanical and Industrial Engineering, Ryerson University. The Pin-on-disk wear test, 3D optical profilometry and indentation experiments were conducted in Dr. Dongyang Li's lab. Analysis of the data presented in chapter 4, conclusion presented in chapter 5 and the literature review presented in chapter 2 are my original research work.

Acknowledgement

First, I want to express my heartfelt gratitude towards Dr. Dongyang Li for his utmost guidance, inspiration and valuable remarks on my work throughout my whole graduate study life. His proper supervision helped me to enrich my knowledge and critical thinking ability about materials and their properties.

I also want to thank Chemical and Materials Engineering faculty and academic staff, technical support staff, post-doctoral fellows and graduate students for their support, assistance and comments. Specially, I would like to thank my colleagues in Dr. Dongyang Li's group. I am very pleased to get the opportunity of working with them. Specially, I would like to thank Dr. Meisam Nouri, Dr. Hao Lu and Dr. Tingzhong Li for their assistance, mentorship and training towards properly conducting my research and academic works. I want to thank Dr. Daolun Chen from Ryerson University, Ontario, Canada for his collaboration in our research. I also want to thank my colleague Vikas Kumar to be always beside me in any circumstances from the beginning of my life in Canada.

I am grateful for financial support from the Natural Science and Engineering Research Council of Canada, Camber Technology Corporation, Suncor Energy, GIW Industries Inc., Shell Canada Ltd., Magna International Inc. and Volant Products Inc.

Above everything, I remember the support I got from my parents to pursue my graduate study in Canada and want to thank them from the core of my heart. I thank my wife, my best friend, who encourages and inspires me daily.

Contents

List of Figures

List of Tables

List of Symbols

W	Wear rate
Z	Number of atoms removed per encounter
P_m	Flow pressure of material
F	Applied Load
S	Sliding distance
H	Hardness
K	Wear coefficient
V	Volume loss
η	ratio of the recoverable deformation energy to the total deformation energy
d	Maximum penetration depth
L_1	Wear load
L_2	Indentation load
K_p	Partial wear coefficient
E	Young’s modulus of tested material
E_r	reduced elastic modulus
E_i	Young’s modulus of conical indenter
ν	Poisson’s ratio of tested material
ν_i	Poisson’s ratio of conical indenter
σ	Von Misses flow stress
σ_y	Yield Stress
K_s	Strength Coefficient
ε_s	Plastic strain
m	Strain hardening exponent
x	Penetration depth of the asperity
a	Radius of the contact area
A	Contact area
A_t	Lateral contact area
α	Fitting parameter in the indentation curve
n	Fitting parameter in the indentation curve
τ	$2/n$

List of Abbreviations

ASTM	American Society for Testing and Materials
PE	Pseudoelasticity
HSLA	High Strength Low Alloy steel
SEM	Scanning Electron Microscope
EDX	Energy Dispersive X-ray Spectroscopy

Chapter 1 Introduction

Surface wear is a phenomenon of material removal when two surfaces slide on each other under a certain normal load, involving deformation, fracture, possible chemical reaction and melting [1]. Resistance of materials to wear is of importance to the reliability of mechanical systems and their performance during service. Wear can result in high costs for repair and replacement of worn components as well as the production loss during machine downtime. One study showed that, tribological contacts contribute to about 23% of the world's total energy consumption. 20% of that is consumed to overcome friction, and 3% of that is used to reproduce the damaged machine parts and equipment because of the wear damage. But this energy loss because of friction and wear could be decreased by 18% within 8 years and by 40% within 15 years by proper selection of materials, with the advance of new surface technology, wear protection and lubrication technology [2]. For this reason, efficiency and safety of machine parts and equipment with longer service life and reduced expense are highly demanded. In order to achieve these goals, factors influencing the wear process and their extent under different service conditions should be properly understood.

Wear of materials is the response of the overall tribosystem. Multiple factors, such as the mechanical properties of the materials, operating condition and geometry of the wearing components influence the wear process. These factors could increase the wear intensity by several orders of magnitude [3].

Wear can occur in several different mechanisms involving abrasion, adhesion, oxidation, fatigue and also possibly more than one mechanism contributing to the wear process in many cases [1]. Thus, accurate prediction of wear rate is challenging [4]. Researchers have been working to develop the wear models and predictive equations. A number of such kind of models and equations for different materials combinations have been published in literature but none of them suits for general use towards precise prediction of friction and wear [5]. Up to date, this situation has not been improved that much. This happens because the information on wear of different materials under different service conditions is very hard to obtain due to the fact that wear is a multi-factor related process. The mutual influences of these factors make wear modeling very difficult.

However, these models and equations can still provide valuable information about proper material pairs under specific service conditions, helping predict their performance for material selection. Archard proposed such an equation in 1953 which is widely accepted for macroscale wear prediction [6]. He suggested that the volume loss of material due to wear is linearly proportional to the normal load and the sliding distance, and inversely proportional to the hardness of the softer material [7]. However, this simple equation is not true in all the experimental cases. For example, Wear loss only changes, more or less non-linearly with the normal load.

The objective of this study is to find out the reason behind this nonlinear relationship between the volume loss and the normal load and how the subsurface strain-hardening influences the wear behavior of materials.

Chapter 2 Literature Review

2.1 Purpose

Over the past few decades, a number of wear models have been developed to predict the wear loss and understand the associated failure mechanism according to the material properties. The principle purpose of this literature review is to understand work that has been done on this topic.

2.2. Wear

Wear means progressively unwanted loss of materials from contacting surfaces. Wear can be defined in several ways. According to American Society for Testing and Materials (ASTM), wear is a – "damage to a solid surface, generally involving progressive loss of material, due to relative motion between that surface and a contacting substance or substances" [8]. The total wear mechanism is complicated and depends on multiparameter such as composition and properties of the surface, contact cycle, surrounding environment and forces involved. When two surfaces come into contact, highly stressed localized contact points are generated. Fracture, shearing, or flow takes place at these concentrated contact points and consequently pieces of the material are removed from the surface and become debris [9]. Under constant load and velocity, the wear proceeds through the repeated contact process.

2.3 Wear Classification

According to appearance, physical mechanism and situation of contact, Bayer classified wear in three ways [10]

2.3.1 Appearance of the wear scar

Worn surfaces may show the following appearances of being polished, scratched, crazed, fretted, pitted and spalled etc.

2.3.2 Physical mechanisms

Wear may involve adhesion, abrasion, delamination, oxidation and a combination of several mechanisms. Figure 2.1 schematically represents a single tribo-event that involves different mechanical, physical, chemical and metallurgical processes under high normal and shear loads.

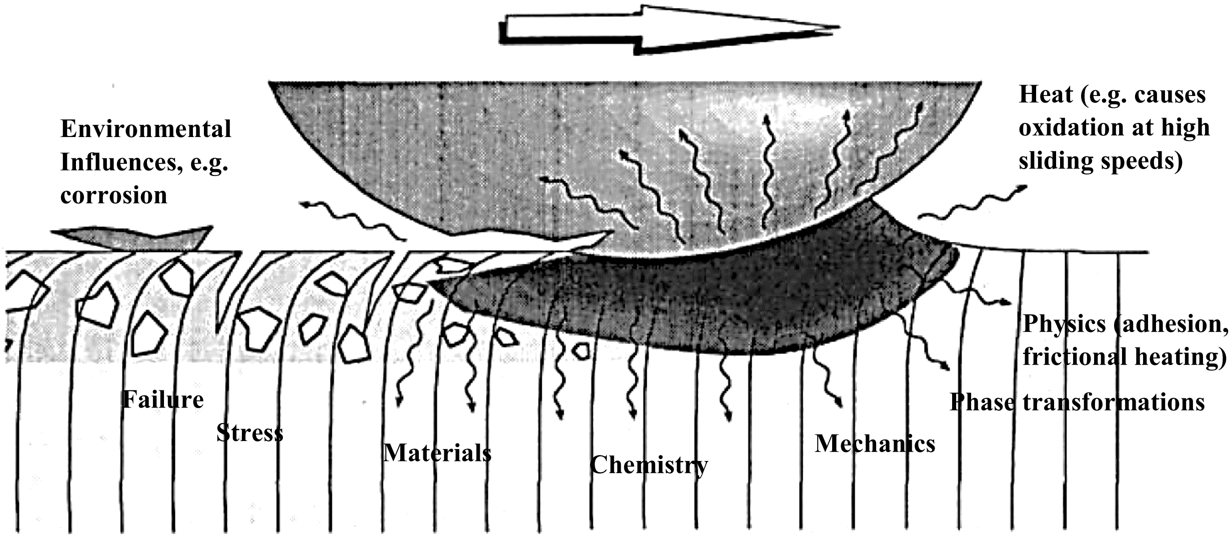

Figure 2.1 Schematic representation of a single tribo-event that transforms the material surface into an active layer under high normal and shear forces by involving different mechanical, metallurgical, physical and chemical processes [11]

2.3.3 Condition of wear

Rolling, sliding, lubricated contact, unlubricated contact, high stress and high temperature etc. are generally considered when the contact conditions are discussed.

Kostetskii et al. in 1976 classified wear based on the reliability of surface performance and the nature of interaction processes [12]. The distinguished classes of wear were: acceptable and unacceptable wear. Acceptable wear included (a) normal mechanochemical oxidative, (b) normal mechanochemical non-oxidative, and (c) mechanochemical form of abrasive wear. Unacceptable wear consisted of (a) seizure, (b) fretting damage, (c) mechanical form of abrasive wear, (d) rolling fatigue (pitting), and (e) other forms of damage, such as corrosion, erosion, cavitation, and crushing.

Kato classified wear mechanism into three major groups: mechanical, chemical and thermal wear. These wear models were further classified into seven different mechanisms [13]

2.3.4 Mechanical Wear

Mechanical wear is referred to wear mainly caused by deformation and fracturing. It includes removal of material by mechanical actions under conditions of sliding, rolling, or repeated impacts. The deformation up to failure dominates the overall wear process of ductile materials, while fracturing commonly plays a major role in the wear process of brittle materials. The mechanical wear includes adhesive wear, abrasive wear, flow wear and fatigue wear.

Among them, abrasive wear and adhesive wear have been taken into consideration in this research.

2.3.5 Adhesive Wear

Adhesive wear is mostly common in nonlubricated or dry contact conditions specially in metals, electrical contacts, product assembly conveyor systems bearings, and gears operating in space vacuum. Adhesive wear of ductile materials refers to wear due to localized bonding between contacting surfaces. As the sliding motion continues, asperities from the softer material will shear off and adhere to the harder material. Once the fragmented asperities are transferred to another surface due to high bonding strength on the interface it may remain at the surface and form a ‘transfer film’, or can form a free forming loose wear particle [14]. The formation of free forming wear particle is possible due to variation of stress acting on a fragment. Severe stress developed at the contact interface and the fragment is deformed elastically. If the stress relief associated with particle leaving from contact zone is stronger than the adhesive bond, then the loose particle forms. Wear coefficients of metals due to adhesive wear are usually between 10^{-7}-10^{-2}, depending on operational conditions and material properties. Adhesive wear mechanism is illustrated in Figure 2.2.

Figure 2.2 Adhesive Wear Mechanism[10]

2.3.6 Abrasive Wear

Abrasive wear is the loss of material by the passage of hard particles or hard surface over relatively soft surface. Tangential force on the target surface exerted by asperities on the counterface causes plastic deformation and eventually material removal. Abrasive grooves can also be found on the wear tracks resulting from sliding between similar metals [15]. Work hardening and third body formation at the interface commonly occur during abrasive wear. Abrasive wear is further classified into 2-body and 3-body abrasion. In the three-body abrasion, hard particles coming from outside are pressed between the surfaces, causing abrasive wear. Whereas in two body abrasion, wear is caused by hard asperities on the counterface. In micro-level, abrasive action involves ploughing, cutting or fragmenting. One of the examples of abrasive wear are the wear of magnetic recording heads by tape. The magnetic particles in the tape act as a very fine abrasive. Abrasive wear mechanism is illustrated in figure 2.3

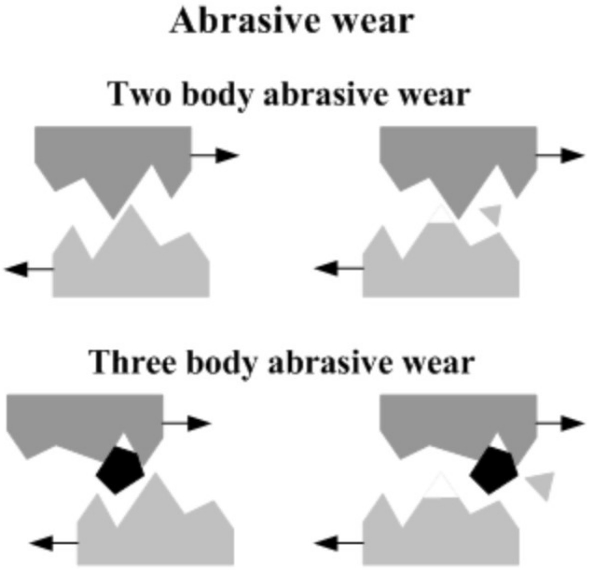

Figure 2.3 Abrasive Wear Mechanism [15]

2.4 Classification of Wear Models

In recent years, research on developing wear models has received increasing interest due to the demand for prediction of wear rates and service life of various industrial facilities suffering from wear. By far, researchers have applied various approaches to understand wear process such as those for fatigue, plastic deformation, oxidation, crack formation and propagation. These factors have been thoroughly studied and relevant theories have also been used to model the wear process.

Wear models reported in the literature may be divided into two principle categories –

(i) Mechanistic models, which are based on material failure mechanism, e.g., ratchetting theory for wear [16]

(ii) Phenomenological models, which predict wear rate based on basic contact mechanics, e.g., Archard's wear model

2.5 Archard's Wear Model:

In this section, Archard's wear model is reviewed and its limitations are discussed -

2.5.1 Review of the Archard's Wear Model:

In the 1950's, researchers first attempted to develop theoretical explanation of the material wear based on the idea upon which the theory of friction was established [17]. The basis of the attempt was the concept that the apparent contact area between two surfaces is far higher than the real contact area. This real contact area can be estimated by determining the amount of localized deformation of the contacting surface asperities under the applied load. During the sliding of the two surfaces against each other, numerous local areas of true contact will form. They will change locations during the sliding process and result in the formation of some local encounters between small regions of the two sliding surfaces. The influence of the amount of these local encounters and their nature was the basis for wear theories.

Holm [18] also proposed a semi-empirical theory of wear, in which he considered the formation of a wear particle an atomic process. According to the theory, during the sliding process between the two surfaces in contact, there is a statistical probability for an atom to get pulled out from its parent surface. Holm considered that material gets removed from the parent, similar to the removal of an individual atom. Based on this concept, he showed that the wear rate W is given by [7] -

$$\boldsymbol{W = ZP/P_m} \tag{1}$$

Where, Z = Number of atoms removed per encounter

P_m = Flow pressure of material

Burwell and Strang however showed that, material removal occurred as removal of large aggregates of atoms, rather than individual atoms. This made Holm's concept of material removal as atoms to be invalid and needed to be modified.

Archard reviewed the above-mentioned research works and proposed a model in 1953 [7], suggesting that, if the asperities undergo plastic deformation under applied load, the wear loss W can be estimated by,

$$\boldsymbol{W = k\frac{FS}{H}} \tag{2}$$

where F is the normal contact force, S the sliding distance, H the hardness of the target material, and K is the wear coefficient which is a dimensionless constant having influences from other factors.

To derive this simple wear model, Archard considered two rules of wear –

a. Wear rate is independent of the apparent contact area

b. Wear rate is directly proportional to the applied load

In this model, the wear rate has a linear relationship with wear rate and the applied load. Archard considered that since the wear rate is independent of the apparent area of contact, an increase in the contact load for the same contact area will increase the wear loss by n times. But Archard also noticed that only some materials show the linear relation between the load and the wear rate and the reason for that was not properly understood.

According to Archard's model, wear rate is inversely proportional to the hardness of the material. This is because, the area of contact is dependent on hardness of the target material and that of the counterface [19].

2.5.2 Exceptions Against the Archard's Wear Equation:

Archard's wear equation shows that hardness is the only material property that determines the wear loss; such estimated wear loss is often consistent with experimental observations [20–25]. However, exceptions exist regarding this matter. For example, the rate of increment in the wear resistance of material with hardness could be altered by different mechanical behaviors of materials such as strain-hardening.

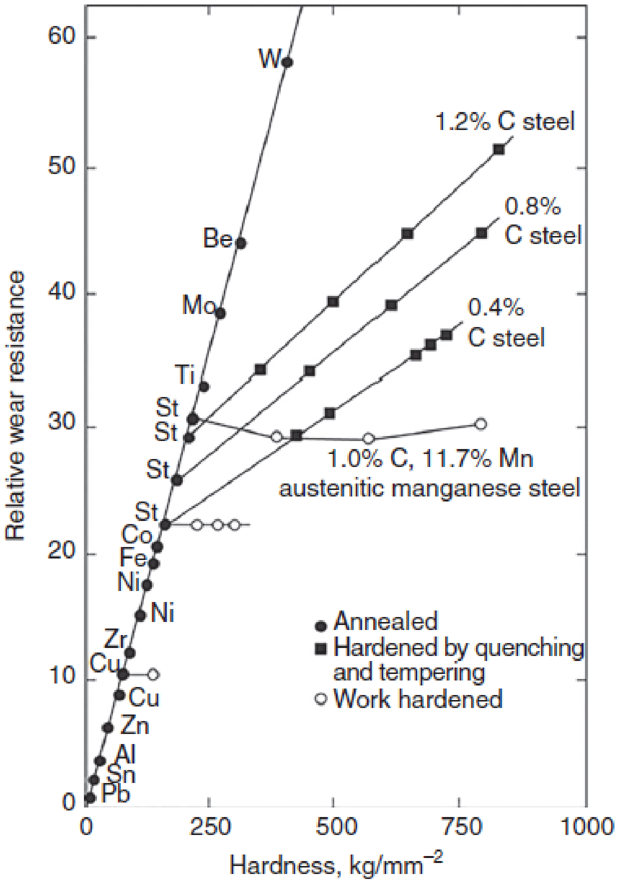

Figure 2.4 Relative wear resistance as a function of hardness for metals and carbon steels worn by abrasive papers [26]

Figure 2.4 represents the relative wear resistance of different pure metals and carbon steels worn by abrasive papers as a function of hardness. As shown, the rate of increment of wear resistance for carbon steels with the increase in hardness is lower than that for the pure metals. Wear rate varies at a higher rate with the intrinsic hardness of the pure metals. While, for carbon steel, its hardness is a combination of its intrinsic hardness of iron and contribution from second phase hardening as well as strain hardening. This increase in hardness by second phase and strain generally reduce the ductility of materials. This reduction in the ductility reduces the material's ability to absorb the deformation energy, which is a measure of toughness of materials [27].

The strain hardening or cold-work particularly lower the toughness. As shown in the figure 2.4 for carbon steel, the increase in hardness by cold-working does not show benefit to the wear resistance of Austenitic Mn steel. This indicates that toughness plays a very important role in determining the wear resistance, especially for hard and less tough materials.

Toughness is usually estimated by calculating the area under the stress-strain diagram which represents the deformation energy that the material can absorb until fracture. Figure 2.5 illustrates the influence of fracture toughness on the wear resistance of materials with varying hardness and ductility [27]. For a certain amount of stress showed by the dashed line in figure 2.5, if there is any fluctuation in localized stress which goes above the yield stress for the material m3, crack will form because of its lower fracture toughness which is represented by the smaller area under the stress-strain curve. On the other hand, the material m1 with the largest ductility and relatively high toughness value will also fail to withstand the same amount of wearing stress because of its poor hardness value. But strong wear resistance can be achieved by having a material like m2 which has the sufficient hardness to support the amount of wearing stress and sufficient fracture toughness to absorb the deformation energy caused by localized impact forces.

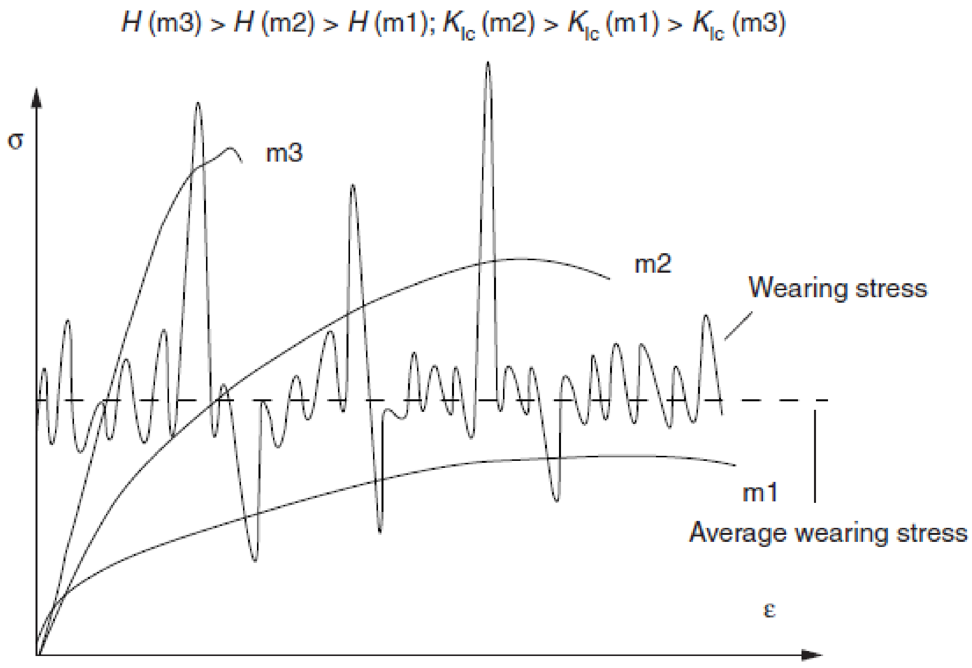

Figure 2.5 Schematic illustration of the stress – strain curves for three different materials. Material m3 has the highest hardness with the lowest toughness value whereas m2 has the highest toughness and m1 has the lowest hardness [27].

It seems that, there should be an optimization between the hardness and the toughness to get the best wear resistance property. This phenomenon has been illustrated more clearly in the figure 2.6 [28]. It depicts the change in the wear resistance with the increment of fracture toughness for several ferrous alloys and ceramic materials. As shown, brittle ceramic materials with lower fracture toughness have poorer wear resistance compared to the ferrous alloys having relatively higher fracture toughness. However, as the fracture toughness increases beyond a certain value at the expense of the hardness, wear resistance decreases with increasing the fracture toughness.

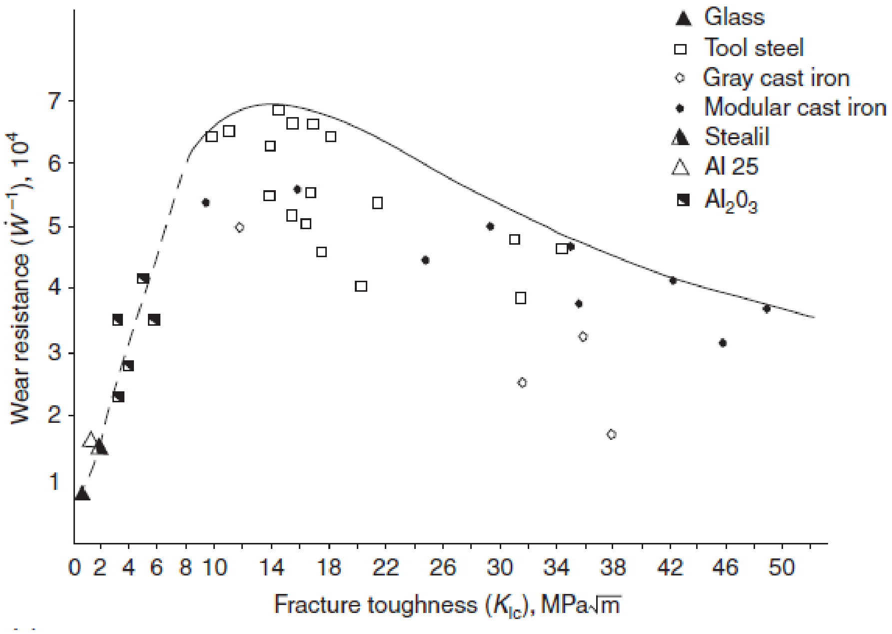

Figure 2.6 Wear resistance vs fracture toughness for different materials [28]

2.6 Previous research works on the modification of Archard's equation:

Although Archard's equation is widely accepted model to predict the wear rate of materials, for many cases, this equation does not always hold true. Researchers have tried to modify this equation to make better prediction for specific cases. In this section, several such models are discussed –

2.6.1 Modification of Archard's equation to estimate wear of highly elastic/pseudoelastic materials:

Liu and Li conducted studies on the wear behavior of pseudoelastic TiNi alloys [29]. Pseudoelasticity results from phase transformation from Austenite to Martensite, induced by stress [30,31]. The stress-induced phase transformation is reversible. As mentioned by the authors, Archard's equation does not hold true to estimate the wear resistance of the TiNi alloy [29].They modified the Archard's model by incorporating the ratio of the recoverable deformation energy to the total deformation energy (η) under the indentation condition in addition to the hardness of the material. These energies include the contributions of both the pseudoelastic effect and the hardness to the wear resistance, whereas Archard's equation contains only hardness as the material property. The volume loss V has been expressed as,

$$\boldsymbol{V} \propto \left(\boldsymbol{\eta}\, \frac{\mathbf{1}}{\boldsymbol{PE}} + (\mathbf{1}-\boldsymbol{\eta})\frac{\mathbf{1}}{\boldsymbol{H}}\right)\boldsymbol{LS} \quad , \quad \mathbf{0} < \boldsymbol{\eta} < \mathbf{1} \tag{3}$$

Where pseudoelasticity (PE) is proportional to the deformation energy recovered after the indenter is released which is also proportional to the product of η and the maximum penetration depth d. So,

$$\boldsymbol{PE} \propto \boldsymbol{d\eta} \tag{4}$$

Since hardness is inversely proportional to the depth of penetration, it can be expressed as [32],

$$\mathbf{H} \propto \mathbf{1/d^2} \tag{5}$$

By putting the values of PE and H into the equation (3), authors finally expressed the volume loss as,

$$\boldsymbol{V} \propto \left(\boldsymbol{k_1}\frac{\mathbf{1}}{\boldsymbol{d}} + \boldsymbol{k_2}(\mathbf{1}-\boldsymbol{\eta})\boldsymbol{d^2}\right)\frac{\boldsymbol{L_1}}{\boldsymbol{L_2}}\boldsymbol{S} \quad , \quad \mathbf{0} < \boldsymbol{\eta} < \mathbf{1} \tag{6}$$

Where, k_1 (nm^3) and k_2 (dimensionless) are constants, L_1 is the wear load and L_2 is the indentation load and S is the sliding distance.

Another purpose of this work was to investigate the generality of this wear loss equation (6) among different types of materials based on experimental results. The authors observed a significant amount of error (~50%) for the pseudoelastic TiNi alloy by estimating the wear loss based on the Archard's model compared to the experimental result. Whereas they achieved better wear prediction by using a modified Archard's equation as shown in the equation (6), compared to the Archard's equation for the different types of sample. They concluded that for the materials with high elasticity/pseudoelasticity, prediction of wear loss using the Archard equation gave considerable error whereas for materials with regular elasticity, the wear prediction using the Archard equation is compliant with experimental result [29].

2.6.2 Abrasive Wear Prediction Based on the Ratio of Hardness to the Reduced Elastic Modulus:

Torrance in 1980, proposed a model of sliding wear caused by a sharp conical indenter, in which the elasticity of material is incorporated into the Archard's wear model [33]. Instead of hardness, this model uses the ratio of hardness (H) to Young's modulus (E) as the primary material parameter. In 1988, Yi-Ling and Zi-Shan also used a similar physical concept for modeling a rolling contact where the abrasive particles are involved [34].

According to the models, wear rate W (m^3/m) can be represented by,

$$\boldsymbol{W = C\frac{F}{H}K_p} \tag{7}$$

Where C is a constant

H = Hardness of the material

F = Applied load

K_p = Partial wear coefficient

Considering the elastic effect, this K_p can be defined by,

$$\boldsymbol{K_p = (1 + K\frac{H}{E})^2} \tag{8}$$

Where K = constant

Both of the models showed good compliance with the experimental results. The reason for this can be attributed to the use of much harder abrasive compared to the test material. If the hardness difference between the abrasive and the test material is low, mechanical properties of the abrasives play a vital role in the wear process and these models fail to comply with the experimental result. For this case, instead of using only the Young' modulus, using a reduced elastic modulus has been observed to give better prediction of wear loss [35].

If the reduced elastic modulus (E_r) is used, then K_p can be relaced by K_p^* then

$$\boldsymbol{K_p^* = (1 + K\frac{H}{E_r})^2} \tag{9}$$

Where E_r can expressed by the relation [36],

$$\boldsymbol{\frac{1}{E_r} = \frac{1-\nu_i^2}{E_i} + \frac{1-\nu^2}{E}} \tag{10}$$

Where,

E_r = reduced elastic modulus;

E_i = Young's modulus of conical indenter;

ν_i = Poisson's ratio of conical indenter;

E = Young's modulus of tested material, and;

ν = Poisson's ratio of tested material

2.7 Relationship Between the Wear Volume Loss and the Normal Load:

As mentioned earlier, Archard's equation relates the material volume loss linearly with the normal force. Archard also recognized that, this proportional relationship did not hold true for all the cases of wear process. However, the reason needed to be studied.

Lorela et al. [37] showed a nonlinear dependence of wear rate on the normal load for hardened microalloyed steel and Q-T 35KB2 steel. They attributed the nonlinear relationship to the wear transition from mild wear to severe wear. Mild wear occurs for sliding surfaces under low load and low sliding speed. This type of wear causes less surface damage and involves the presence of a tribo-layer rich in oxygen content. On the other hand, severe wear causes immense damage to the surface and is associated with a large amount of material transfer to the counterface [38]. Transition of wear regime from mild to severe wear can be characterized by the change in the contact nature. This depends on the balance between two opposing processes [39]–

a) Exposure of the sliding surface because of the plasticity dominated deformation process
b) Rate of oxidation of the fresh exposed surface because of the surrounding atmospheric condition

During the mild wear regime, contacting surfaces keep separated by the oxide layer resulting from the frictional heating at the counterfaces in unlubricated conditions under low loads. This layer acts as a solid lubricant since it reduces the contact between the sliding asperities, limiting the growth of asperity junction and preferring the oxide-oxide junctions for any crack propagation [40], resulting in low wear rate. Typically, mild wear is characterized by smooth surface morphology with some fine oxide debris.

On the other hand, this protective oxide layer gets removed with the application of higher loads beyond a certain limit and high sliding speed, resulting in extensive metallic contact over the whole real contact area in the severe wear regime. Because of this, severe wear is characterized by rough and heavily deformed worn surface having coarse metallic flake like wear debris. Wear rate is 100 to 1000 times higher in the severe wear regime compared to mild wear regime [39]. Thus the wear loss ~ load relationship can deviate from the linear relation due to the changes in the wear regime [41–43].

However, authors have also reported the non-linear variation of wear loss with normal force in literature. During block-on-disk wear tests on the AZ91 Mg alloy, performed by Chen and Alpas [44], they observed that the slope of the wear rate versus normal load curve gradually increased in the load range of 1 ~ 350 N at low sliding speed within the mild wear regime. A similar phenomenon was also observed with a reciprocating sliding wear test for a commercial low carbon steel with 0.11% C in both original and surface mechanical attrition treated state in the load range of 2 ~ 8N [45]. A power relationship, $W=CF^m$, appeared to well describe the wear behavior of Al-18.5% Si (A390) alloy [46], where W is the wear rate, C is the wear coefficient, F is the normal load and m is wear exponent. Although it is noticed that materials often show non-linear relationship between the material loss and normal force, away from Archard's wear equation, the mechanism is not well clarified.

The non-linear relationship should be ascribed to properties of the target material, e.g., the strain hardening, since it certainly influences the wear behavior [47].

2.8 Subsurface Strain Hardening on Sliding Wear:

In this section, phenomenon of strain hardening under the sliding surface during sliding wear is described -

2.8.1 Overview of Strain Hardening:

Strain hardening refers to the strengthening of a material by plastic deformation. Plastic deformation in metallic crystal lattice is associated with microscopic defects called dislocation. Strain hardening during plastic deformation happens because of the interactions between adjacent dislocations. Dislocations are usually formed by the variation in local stress fields within the material, which cause atomic rearrangement in the crystal lattice by the dislocation movement through the lattice. Dislocations can also be generated through dislocation multiplication [48]. With increased dislocation movement, they accumulate and interact with one another. This generates numerous pinning points within the lattice which hinder the dislocation motion, leading to the strengthening of materials with an increase in yield strength and a decrease in ductility.

A material's strain hardenability can be explained from the tensile stress-strain diagram. Plastic strain region from the stress-strain curve is usually expressed by the power law relation [49],

$$\boldsymbol{\sigma = K_s \varepsilon^m} \text{ for } \boldsymbol{\sigma > \sigma_y} \tag{11}$$

Where σ = Flow stress

σ_y = Yield Stress

K_s = Strength Coefficient

ε = Plastic strain

m = Strain hardening exponent

2.8.2 Mechanism of Strain Hardening During Sliding Wear:

In modeling the sliding wear, Archard did not take account of variations in hardness during the sliding wear process. As a matter of fact, the wearing force causes large amount of shear strain in the surface layer. This shear strain gets reduced with the increase in depth into the bulk of the material [39]. The strain hardening at the sliding surface could cause the hardness to increase two to three times, compared to the bulk hardness of materials. However, the exact value of hardness in the deformed region also depends on material behavior, surrounding temperature, and the strain rate.

2.8.3 Dependence of Strain Hardenability on the Crystal Structure of Materials:

Strain hardening depends on the increase in dislocation density during cold work. Dislocation movement does not occur on all the crystallographic planes and in any direction. They generally move on the closed packed planes within the crystal lattice and move in the closed packed directions. These planes and directions form the so-called slip system. The number of slip systems varies with the crystal structure. With increased number of slip systems, ductility and the rate of strain hardening increase.

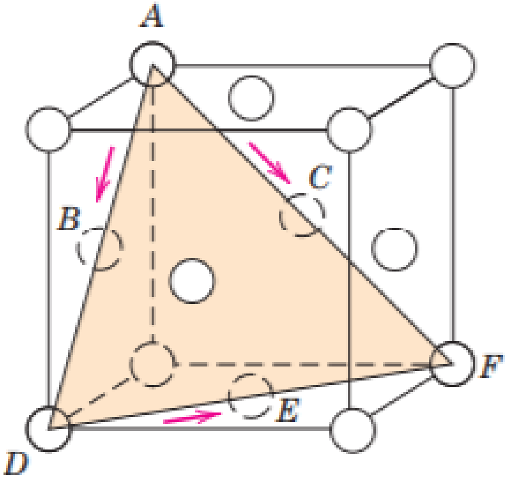

Figure 2.7 Slip system in FCC metals [50]

Figure 2.7 shows the unit cell of a FCC crystal structure with (111) crystal plane. In FCC structure, slip occurs on the {111} close packed planes in <1$\bar{1}$0> directions. As shown by the arrows in the figure 2.7, each {111} type plane contains three different independent <110> slip directions. There are four {111} slip planes available in the FCC crystal structure, leading to 12 slip systems for FCC crystals.

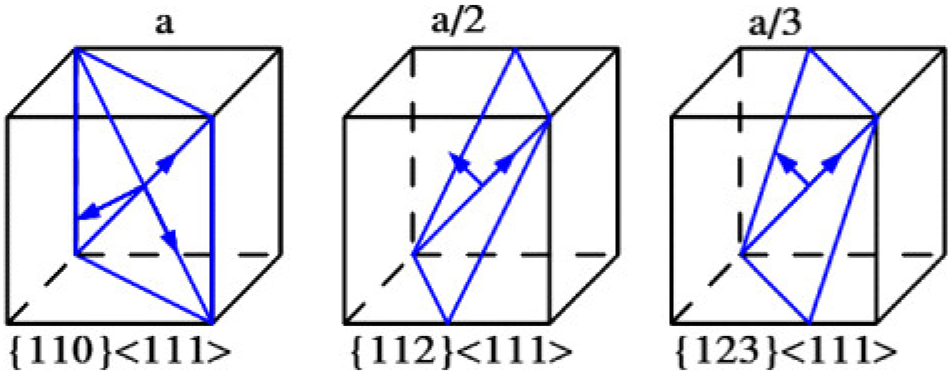

Figure 2.8 Slip system in BCC metals [51]

In BCC crystals, slip occur on several groups of planes with the shortest Burgers vector because there are no truly close packed planes in the BCC lattice. As shown in the Figure 2.8, slip in BCC occurs on the {011}, {112} and {123} slip planes in <11$\bar{1}$> type directions within each slip plane. In BCC, there are six {011} type slip planes with 2 <11$\bar{1}$> type slip directions, 24 {123} and 12 {112} type slip planes each having one <11$\bar{1}$> type slip direction. That means, for some BCC materials, there can be 48 different types of slip systems available [52]. With the larger numbers of available slip systems, FCC and BCC materials are relatively ductile since extensive plastic deformation is possible with these slip systems.

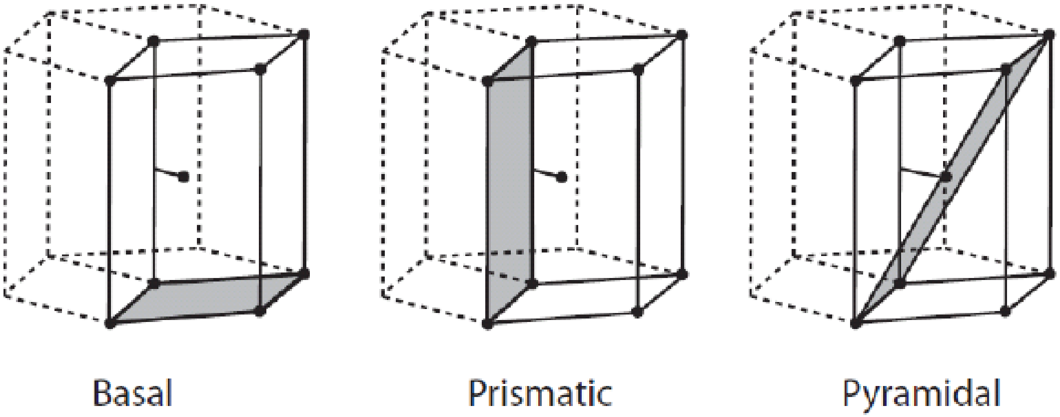

Figure 2.9 Slip systems in HCP metals and alloys [53]

Unlike the BCC and FCC, Hexagonal close packed (HCP) structures have very few slip systems. Usually slip occurs in HCP in the basal {0001} plane along the <11$\bar{2}$0> directions. Other slip planes can be available like {10$\bar{1}$0} prismatic slip plane and {10$\bar{1}$1} pyramidal slip plane (Figure 2.9) but activation of these slip planes depends on other parameters such as the c/a ratio. There are only two independent slip systems available with the basal {0001} plane. For plastic deformation to occur, activation of additional slip systems or twinning is required. This makes HCP materials brittle in nature.

2.9 Main Objectives of This Study:

Archard's wear equation is widely used in industry for preliminary selection of materials against wear mainly based on their hardness. According to the equation, the material wear rate is linearly proportional to the contact force. However, it is often observed that the material loss increases nonlinearly with the contact force in a small load range without involving any wear regime transition. Thus, the non-linear relationship should also result from variations in basic mechanical behavior of materials such as strain-hardening capability during wear. In order to improve the accuracy for wear rate prediction and material selection, this study is conducted

1) to investigate the material loss – contact load relationships for three selected alloys with typical metallic crystal structures: FCC, BCC and HCP;
2) to understand the non-linear wear ~ load relationship and extract additional information on the material behavior from the non-linear material loss ~ contact load relationship;
3) develop an analytic model to quantitatively link the non-linearity with the material's indentation behavior.

Chapter 3 Experimental Procedure

3.1 Sample Preparation

For our study, three types of samples with dimension 25 mm x 5 mm x 3 mm were used –

1. 5182 Al alloy
2. AZ31 Mg alloy
3. High Strength Low Alloy (HSLA) Steel

Compositions of these samples have been provided in table 3.1

Table 3.1 Compositions Al-5182 alloy, AZ31B Mg alloy and HSLA

Sample	Composition
Al-5182	Al 93.2-95.8%, Cr 0.1%, Fe 0.35%, Mg 4-5%, Mn 0.2-0.5%, Si 0.2%, Ti 0.1%, Zn 0.25%
Mg-AZ31B	Mg 97%, Al 2.5%-3.5%, Ca 0.04%, Cu 0.05%, Fe 0.005%, Mn 0.2%, Ni 0.005%, Si 0.1%, Zn 0.6-1.4%
HSLA	Fe 98.7%, C 0.15%, Cu 0.2%, Mn 1.0%, P 0.15%, S 0.05%

The samples were polished using 180, 400, 600, 800 and 1200 grit abrasive sandpapers, and rinsed with acetone ultrasonically. After that, all three samples wear subjected to pin-on-disk wear test.

3.2 Wear Test

Dry sliding wear test of these samples were performed using a pin-on-disc wear tester made by the CSEM Instruments, Peseux, Switzerland (figure 3.1) in agreement with the ASTM G99-17 standard [54]. A schematic illustration of the pin-on-disc tribometer has been shown in fig. 3.2. Here, wear on the sample surface is created by placing the sample on a rotating disc and simultaneously applying a load on a pin that is in contact with the sample surface.

All the samples were subjected to normal loads of 1N, 2N, 3N, 5N, 7N, 10N, 12N and 15N. The pin used for wear test was a Si_3N_4 ball of 3 mm in diameter. All the tests were conducted at a sliding speed of 1 cms^{-1} along a circular path of 1 mm in radius for 3000 revolutions or 18.84 m sliding distance under room temperature and 50% humidity. Air flow was directed to the sample surface during the wear test to maintain constant surface temperature. Change of Coefficient of friction with sliding distance was measured in situ.

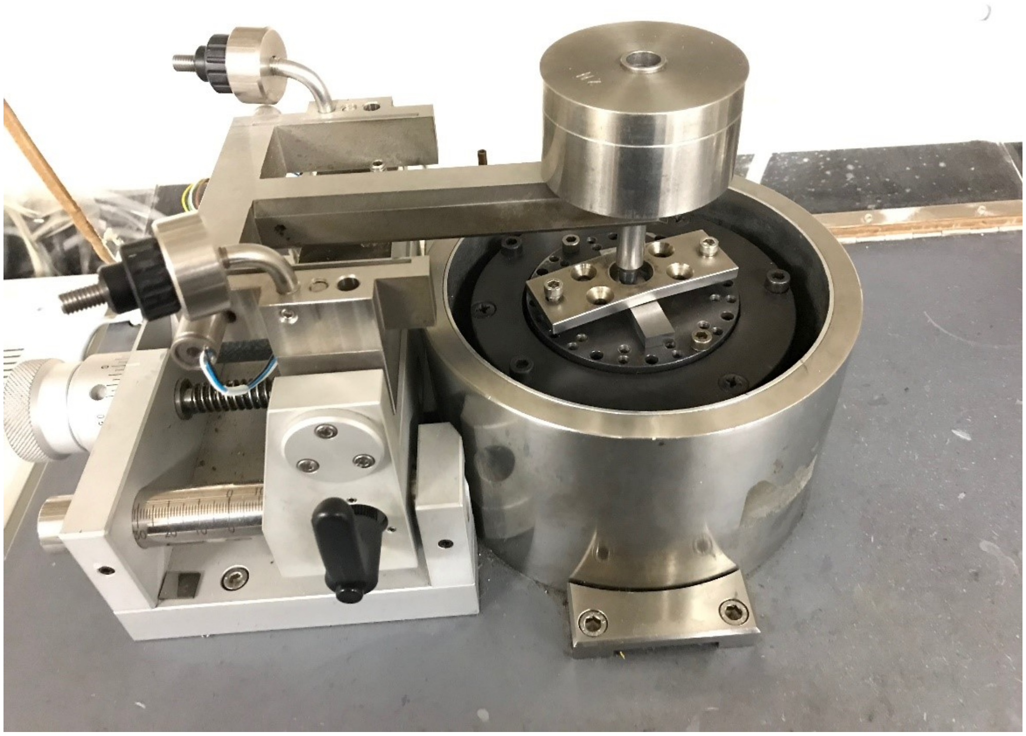

Figure 3.1 Pin-on-disk high temperature tribometer made by CSEM Instruments, Peseux, Switzerland

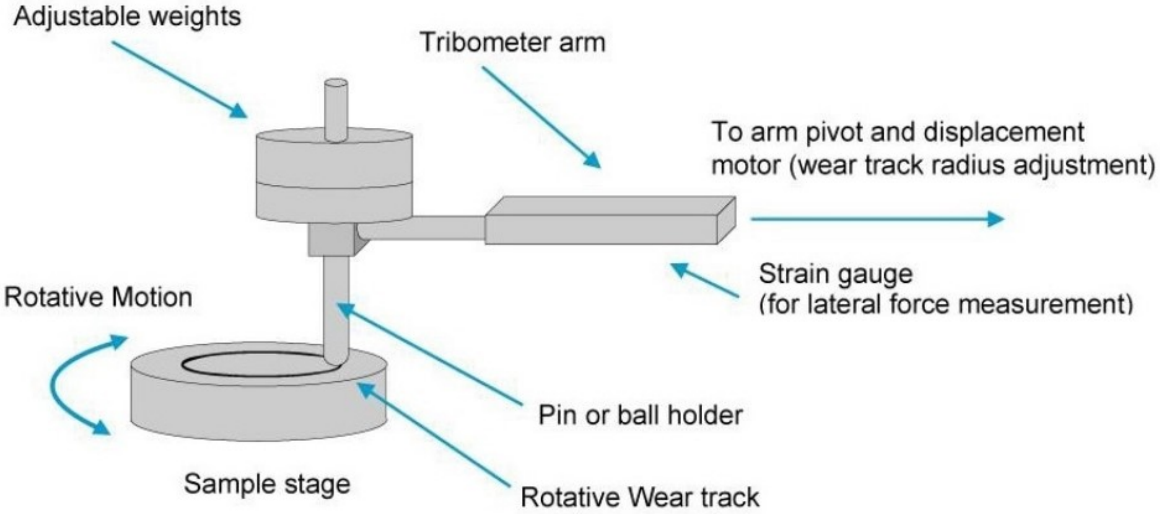

Figure 3.2 Schematic illustration of sliding wear test on a pin on disk tribometer [55]

The worn surface was scanned using ZeGage™ 3D Optical Surface Profilometer (figure 3.3) from which the corresponding wear volume loss was measured.

Figure 3.3 ZeGage™ 3D Optical Surface Profilometer

A schematic illustration of the principle of a typical 3D optical profilometer has been shown in fig. 3.4. Optical profilometers are basically interference microscopes where the wave properties of light are utilized to measure the height differences on a surface from which the wear loss can be estimated. As shown in fig. 3.4, a light beam is split by a beam splitter inside the optical profilometer. Half of the split beam is reflected from the test material surface and passed through the focal plane of the objective. The rest of the split beam is reflected from the reference mirror. These two reflected beams then combine at the beam-splitter, causes interference fringes based on the difference in the wavelengths of the light beams and reaches the camera. The optical path difference between the test surface and a reference surface is estimated from the interference pattern and compared to measure the height variations on the surface [56,57]. For sliding wear, this height variation gives the depth of the wear track from which, the wear loss is measured by analyzing the wear track in the software.

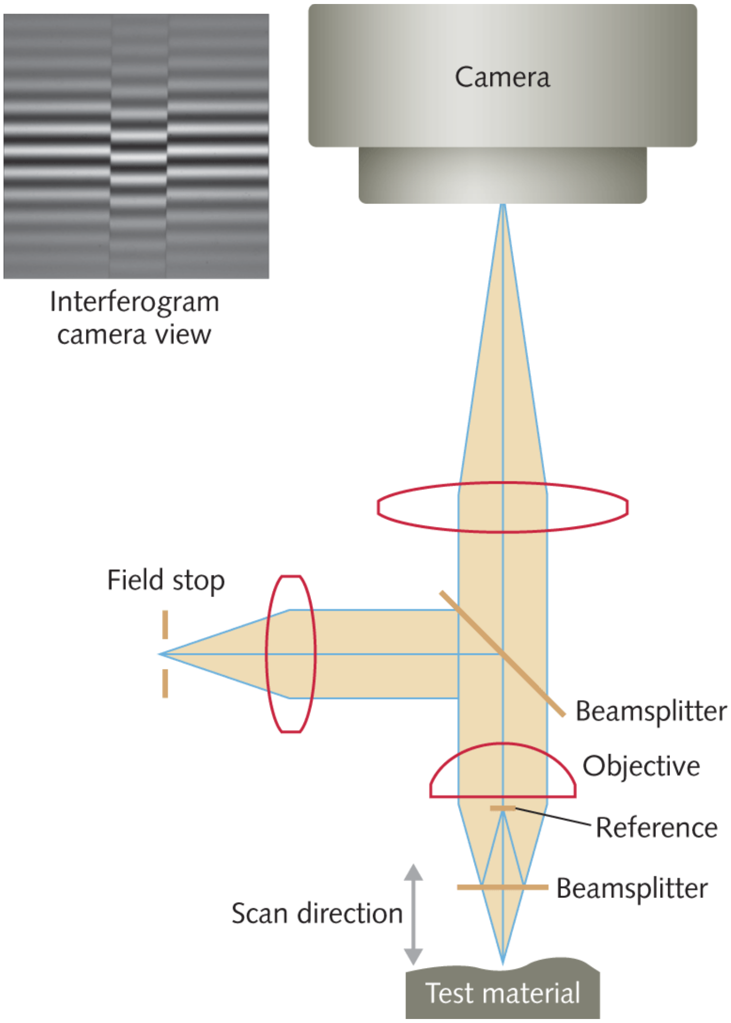

Figure 3.4 Schematic representation of the principle of interferometric 3D optical profilometer operation [57]

3.3 Micro-Hardness Test

Micro-indentation of the samples was performed using a Vickers micro-hardness tester (Fisherscope H100C Microhardness Measurement System with WIN-HCU software) (figure 3.5) with a maximum contact load of 500 mN and applied for 20s from which the hardness of the samples was measured. A cone shaped diamond indenter tip was used for this purpose. Force versus indentation depth diagrams were obtained and the tests were repeated at least three times in different locations for all three samples.

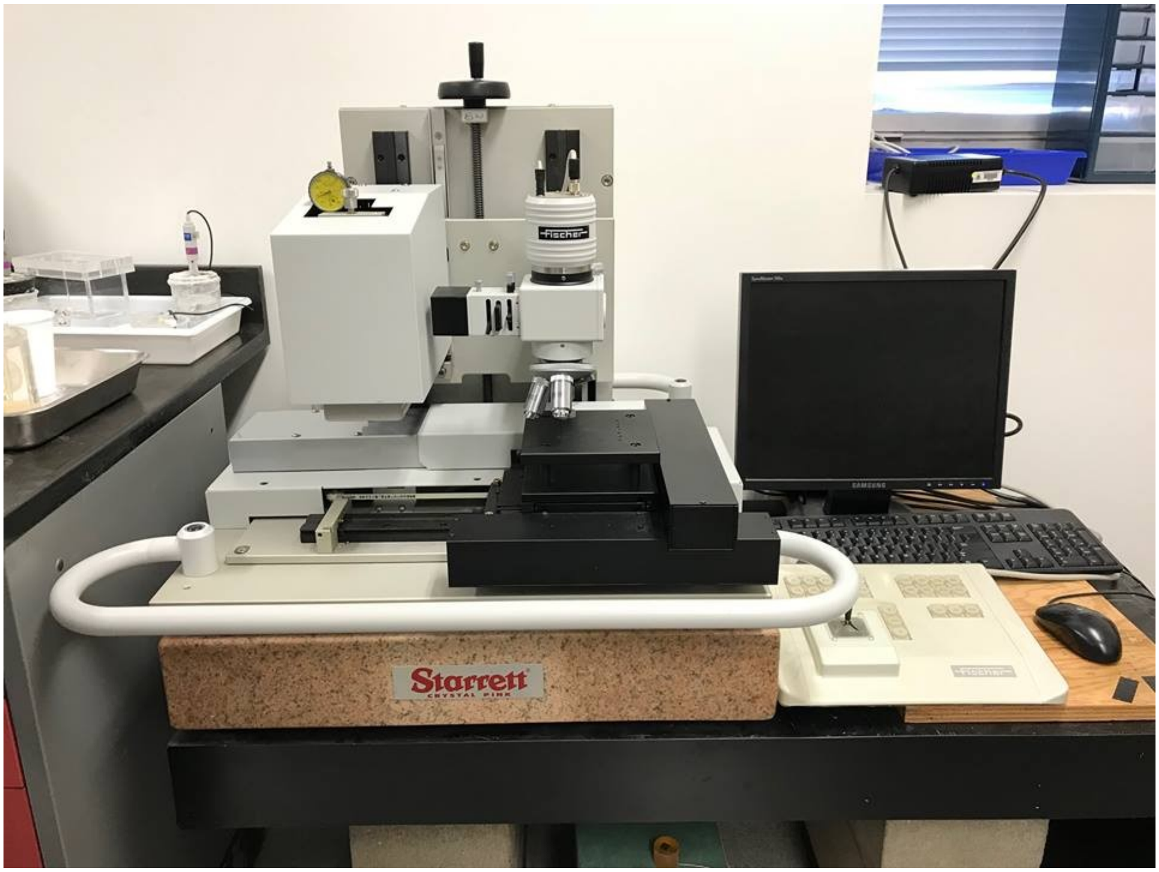

Figure 3.5 Vickers micro-hardness tester (Fisherscope H100C Microhardness Measurement System with WIN-HCU software)

3.4 Microstructure Test

Worn surfaces were subjected to Scanning Electron Microscopy (SEM) analysis using Zeiss Sigma 300 VP-FESEM (figure 3.6), Germany with an Energy Dispersive X-ray Spectroscopy (EDX) attachment. Compositional analysis of the worn surfaces was conducted by taking EDX spectrum at different points on the worn surface.

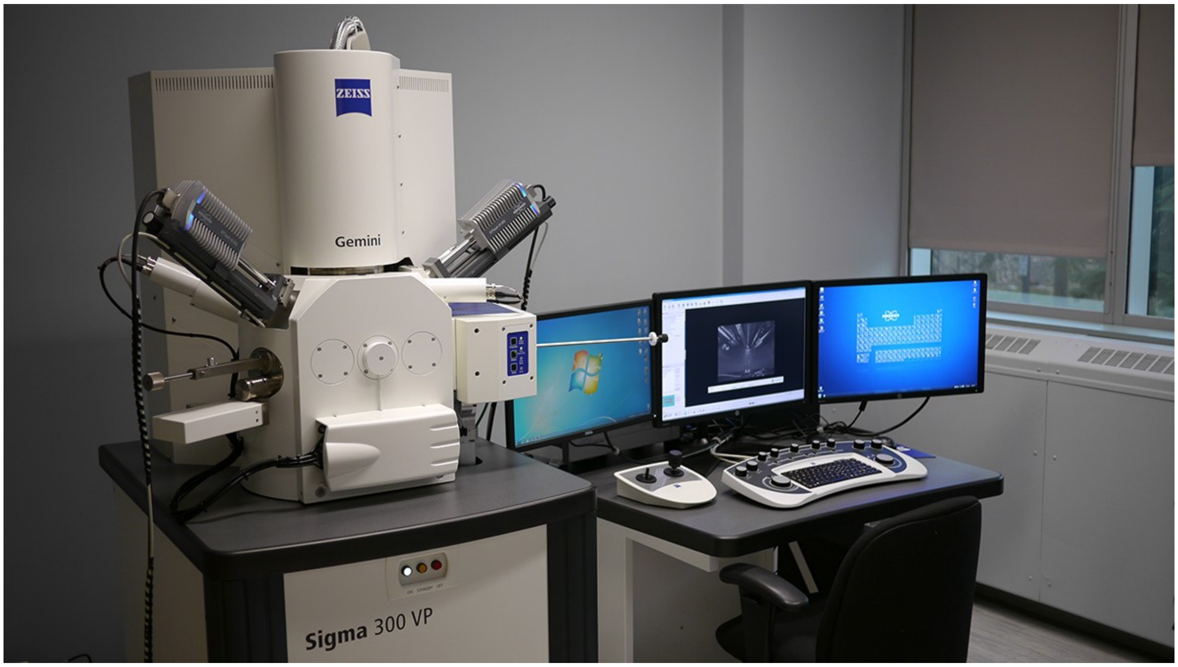

Figure 3.6 Zeiss Sigma 300 VP-FESEM with EDX attachment

Chapter 4 Results and Discussions

4.1 Material loss with respect to the normal force

Volume losses of Al-5182, AZ31B Mg and the HSLA were evaluated using the pin-on-disk tribometer. Figure 4.1 illustrates variations in volume loss of the three alloys with respect to the applied normal load in the range of 1 to 15N over the total sliding distance of 18.84 m. The results show that HSLA has the highest wear resistance while the AZ31 Mg alloy has the lowest one. The Al alloys shows a mediate wear resistance. The wear resistance of the alloys is apparently governed by their hardness. Hardness values of the steel, Mg and Al alloys are 1986.8, 898.0 and 819.8 N/m^2 respectively. As shown, the higher the hardness, the larger the wear resistance.

As shown in Figure 4.1, the volume loss increases nonlinearly with increasing the normal force. The nonlinear relationship is not compliant with the Archard's wear equation. According to Archard's equation, hardness is the determining material property that influences the wear behavior of materials. Thus, it is expected that the hardness varies with the wearing force due to the effect of strain hardening, and the contact geometry may also influence the wearing condition. In order to analyze the issue quantitatively, we propose a model, described in the next section.

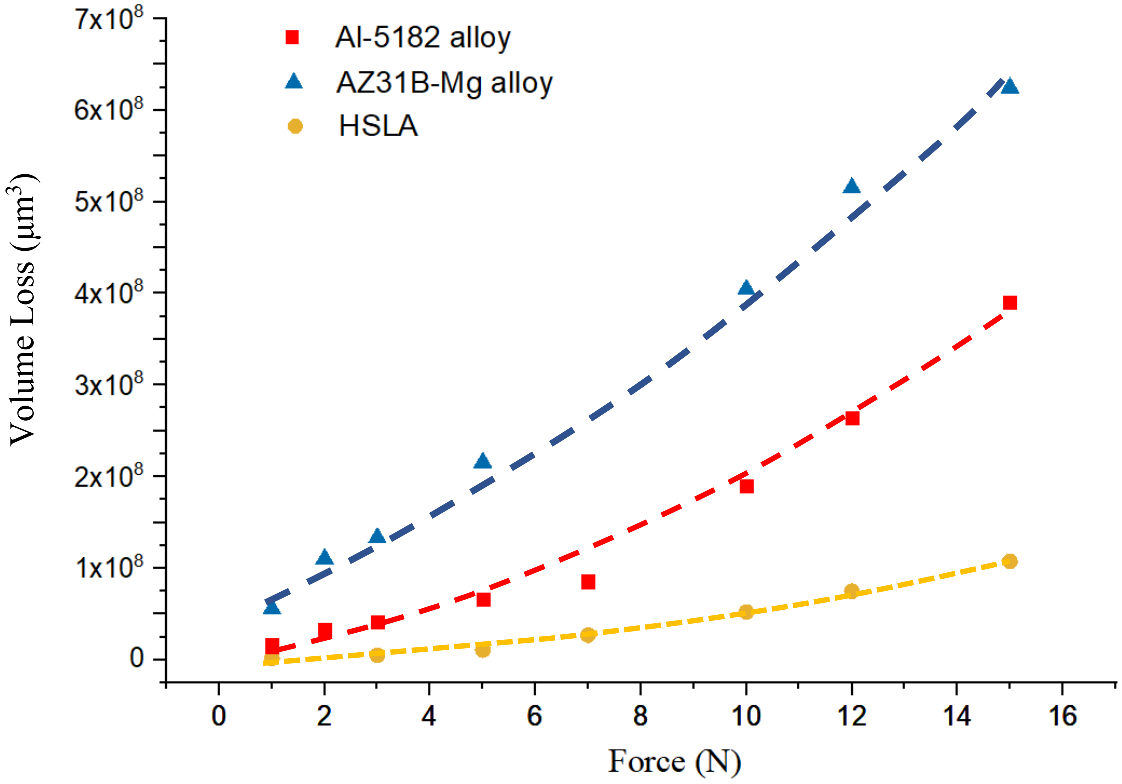

Figure 4.1 Volume loss vs normal load curves of 5182 Al alloy, AZ31 Mg alloy and HSLA under 1 cms-1 sliding speed for 3000 sliding cycles. (Average percent deviation from mean for Al 5182 = 15.1%, for AZ31 Mg alloy = 6.6% and for HSLA = 15.0%)

Possibility of the change in wear regime may exist as the contact force increases. If such changes occur, the variations in volume loss with respect to the contact force could be abrupt or the trend of volume loss ~ force relationship could alternated. However, the contact forces used in the present study varied in a relatively small range from 1N to 15N. Transition of wear regime unlikely occurred. The wear loss ~ load curves shown in figure 4.1 are smooth and do not show such transition, which could be reflected by abrupt changes in slope of wear ~ load curve or wear rate ~ load curve [3,58]. For further information, worn surfaces of the samples were examined using SEM and compositions of selected areas were analyzed using EDX.

4.2 SEM and EDX Analysis:

Figures 4.2 - 4.4, figures 4.5 - 4.7 and figures 4.8 - 4.10 show worn surfaces of 5182 Al, AZ31B, and HSLA caused by contact forces of 1 N, 10 N and 15 N, respectively. Results of corresponding EDX analysis of composition, including oxygen content, in two spots for each sample are provided.

As shown in figure 4.2, the wear track of Al-5182 alloy under 1 N normal load is relatively smooth with shallow grooves along the sliding direction. Some fine debris particles rich in oxygen content can be observed on in the worn track.

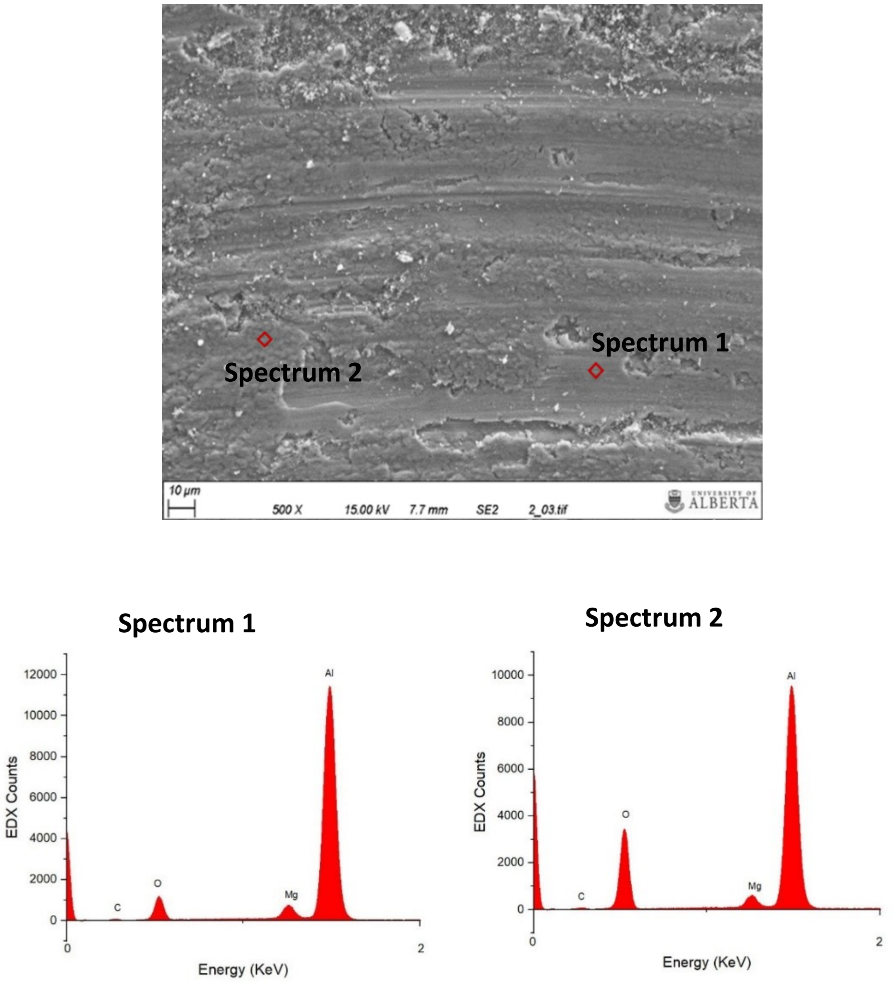

Figure 4.2 SEM and EDX microanalysis of the worn surface of 5182 Al alloy under 1 N load for 18.84 m sliding distance at 1 cms^{-1} sliding speed

Figure 4.3 shows the wear track of the Al-5182 alloy under 10 N load. Under the larger load, the worn track shows similar morphology and fine oxide-rich wear debris.

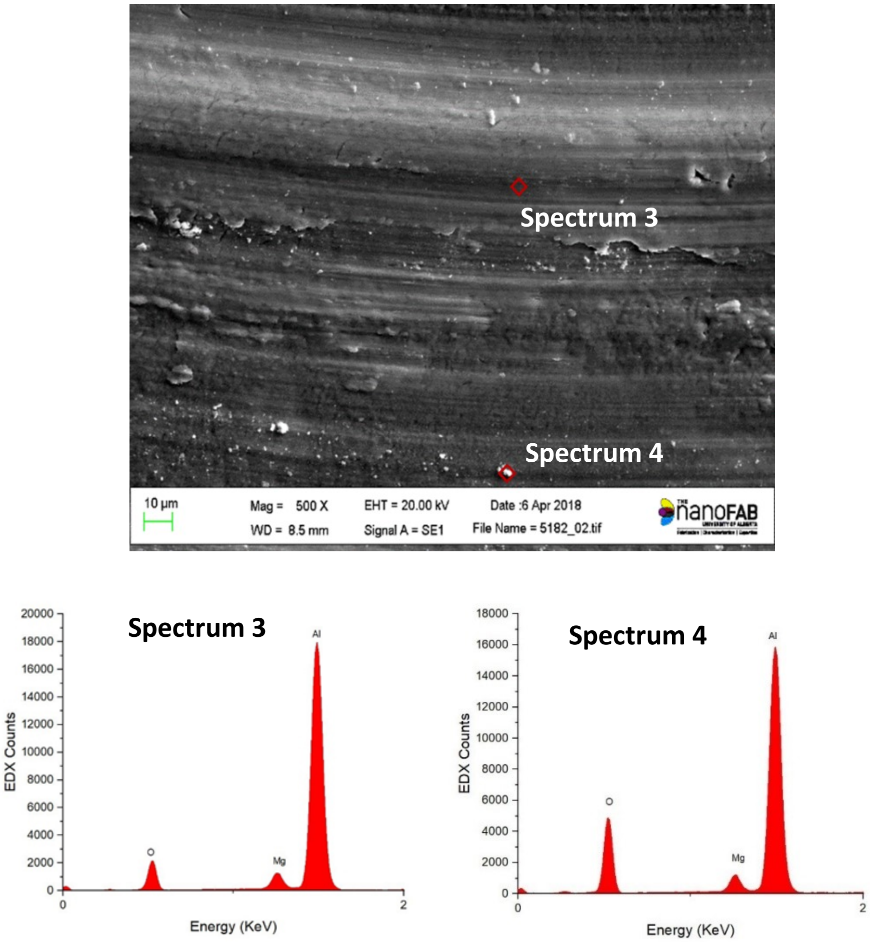

Figure 4.3 SEM and EDX microanalysis of the worn surface of 5182 Al alloy under 10 N load for 18.84 m sliding distance at 1 cms^{-1} sliding speed

Application of 15N load on the sliding wear of Al-5182 alloy also does not show any signnificant change in the wear track (figure 4.4). After increasing the load from 1N to 15N, the surface morphology is still smooth with some fine oxide debris. No characteristic feature of severe wear mechanism like severe plastic deformation, cracks, surface melting has been observed which means that no wear regime transition from mild to severe wear has occurred under the presented wear test condition for the Al-5182 alloy.

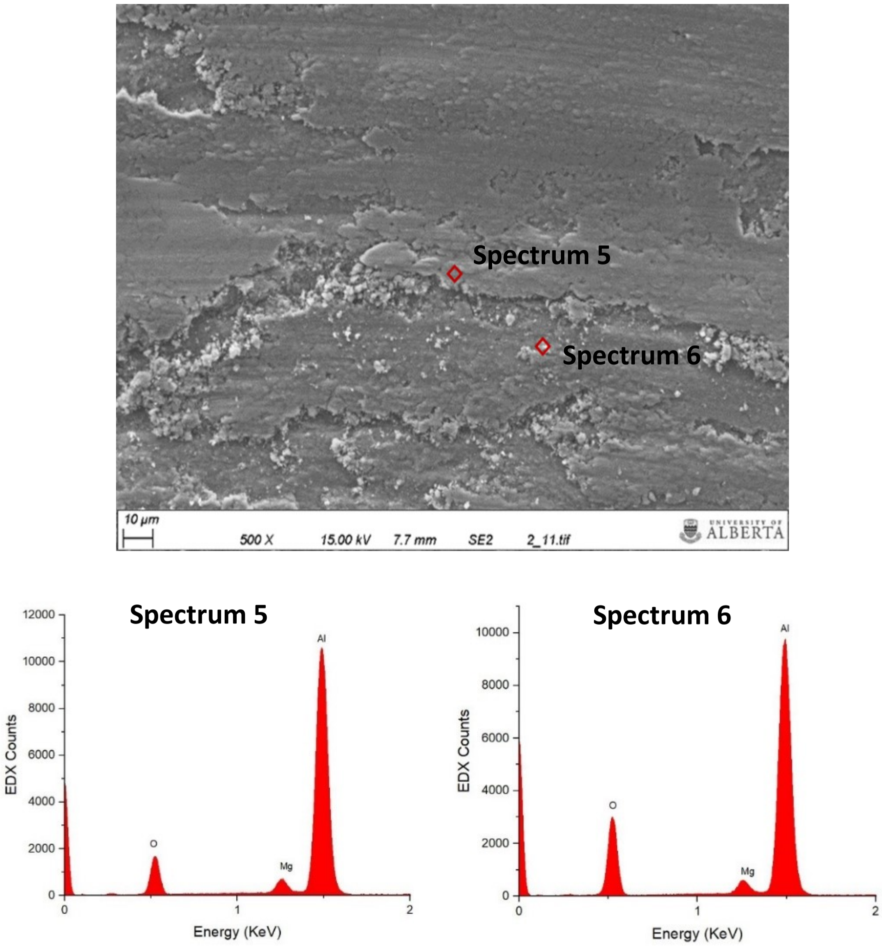

Figure 4.4 SEM and EDX microanalysis of the worn surface of 5182 Al alloy under 15 N load for 18.84 m sliding distance at 1 cms^{-1} sliding speed

Figure 4.5 shows the wear track of AZ31B-Mg alloy under 1N load for 18.84 m sliding distance at 1 cms^{-1} sliding speed. Similar to the Al-5182 alloy, Mg AZ31B alloy also shows relatively smooth worn surface with abrasive grooves and oxygen-rich wear debris.

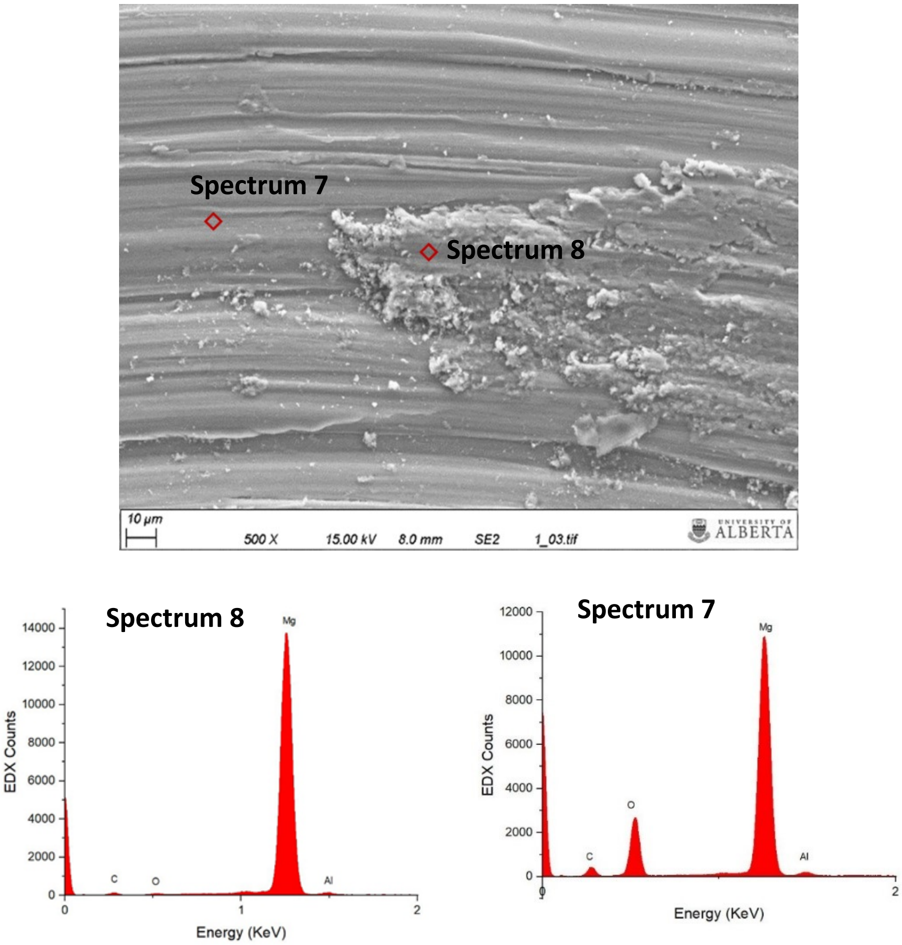

Figure 4.5 SEM and EDX microanalysis of the worn surface of Mg AZ31B alloy under 1 N load for 18.84 m sliding distance at 1 cms^{-1} sliding speed

Figure 4.6 shows the wear track of AZ31B-Mg alloy under 10N load with the same sliding condition as that for 1N. No significant change has been observed after increasing the load from 1N to 10N.

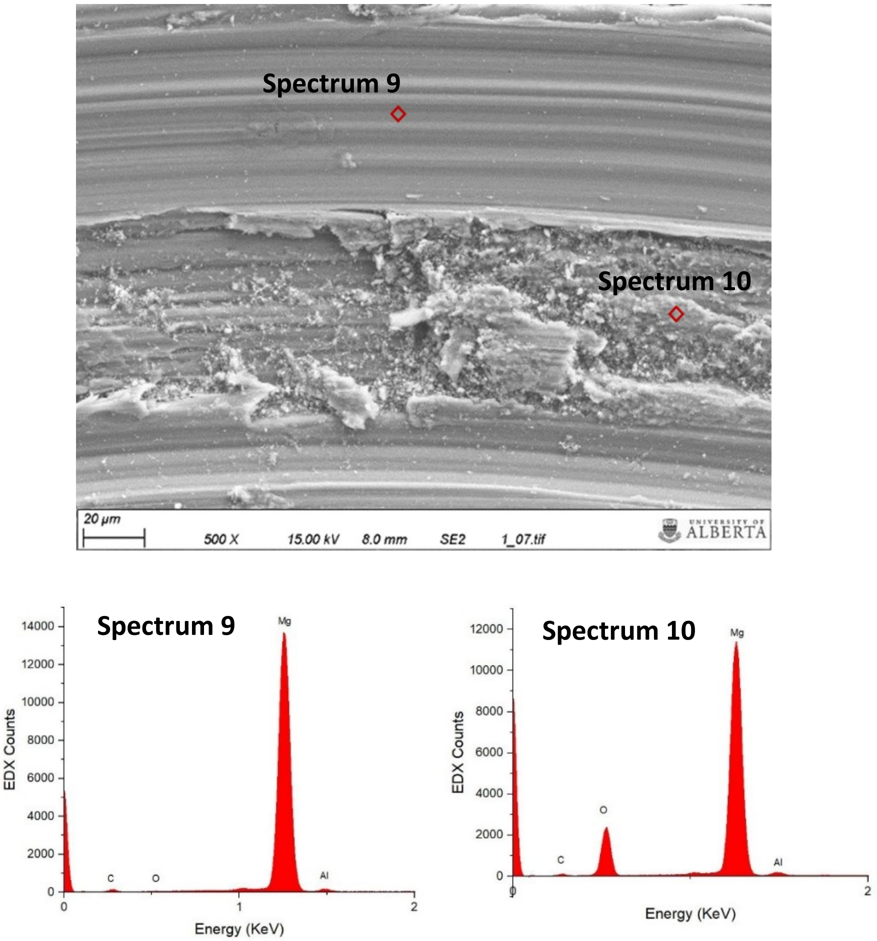

Figure 4.6 SEM and EDX microanalysis of the worn surface of Mg AZ31B alloy under 10 N load for 18.84 m sliding distance at 1 cms^{-1} sliding speed

Figure 4.7 shows the wear track of AZ31B-Mg alloy under 15 N load. It shows that, worn surface is still relatively smooth with some patches of oxide debris, similar to the worn tracks caused by loads of 1N and 10N. No characteristic features of severe wear damage are not observed under the different loads, meaning that no wear-regime transition occurred for the AZ31B-Mg alloy under the present sliding condition.

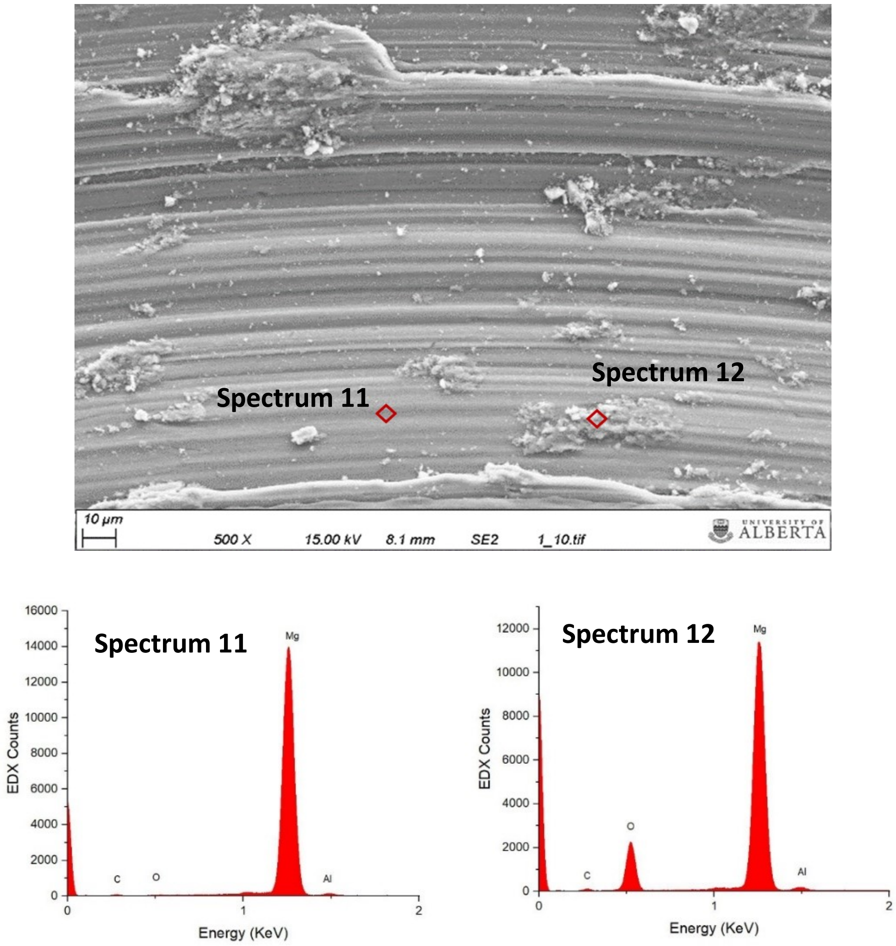

Figure 4.7 SEM and EDX microanalysis of the worn surface of Mg AZ31B alloy under 15 N load for 18.84 m sliding distance at 1 cms^{-1} sliding speed

Figure 4.8 shows the wear track of HSLA under 1N normal load for 18.84m sliding distance at 1cms^{-1} sliding speed. Similar to Al-5182 and AZ31B Mg alloy, the surface morphology is smooth with abrasive grooves and fine debris particles rich in oxygen content.

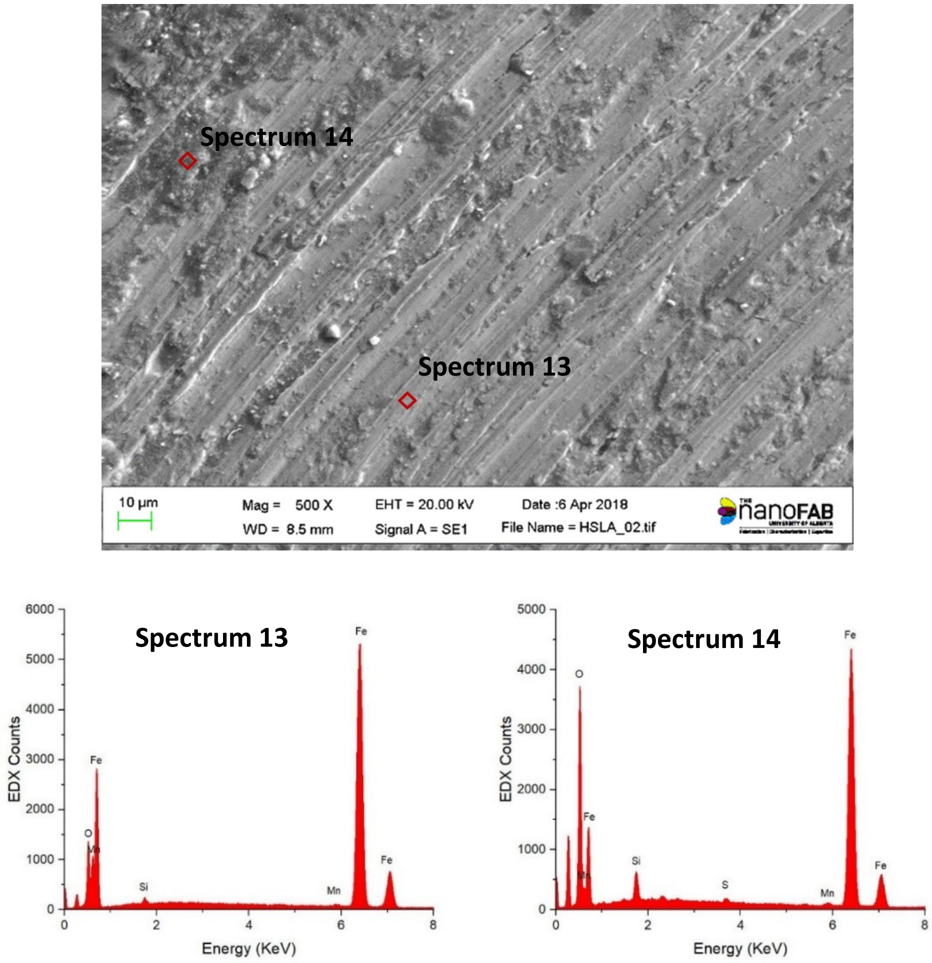

Figure 4.8 SEM and EDX microanalysis of the worn surface of HSLA under 1 N load for 18.84 m sliding distance at 1 cms^{-1} sliding speed

Figure 4.9 shows the wear track of HSLA under 10N load for the same sliding condition as that of 1N load for HSLA. No significant change in wear track was observed after increasing the load from 1N to 10N.

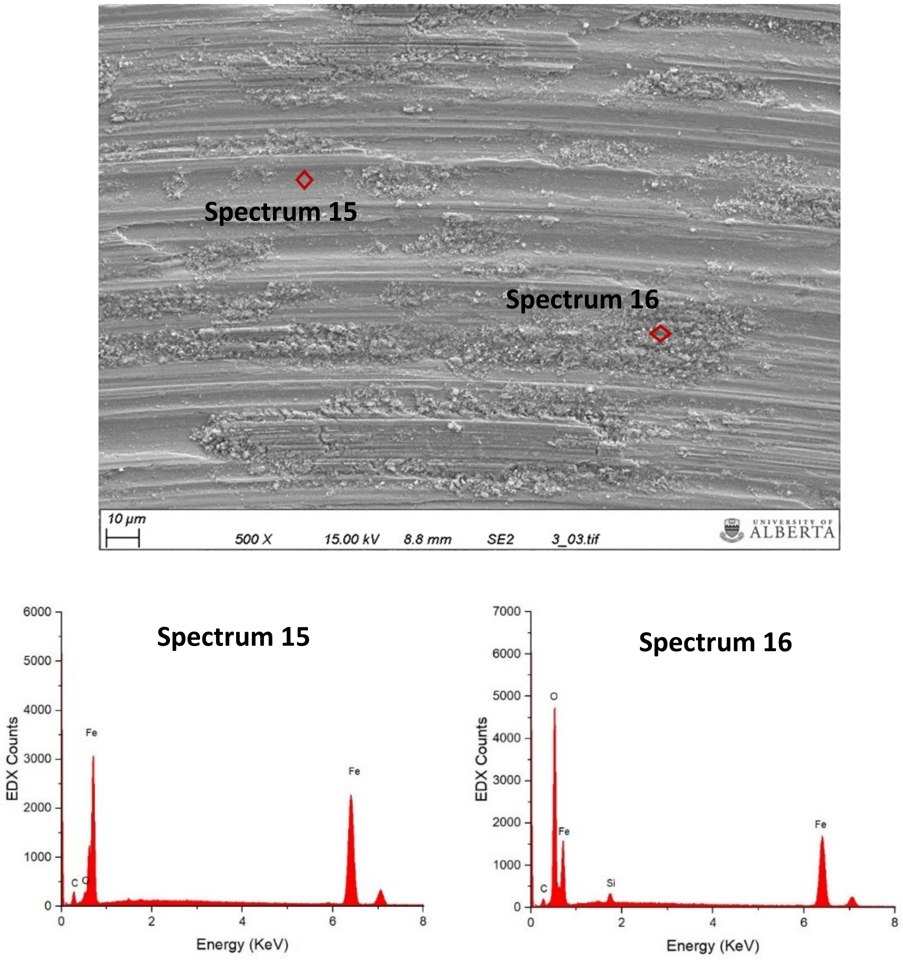

Figure 4.9 SEM and EDX microanalysis of the worn surface of HSLA under 10 N load for 18.84 m sliding distance at 1 cms^{-1} sliding speed

Figure 4.10 shows the wear track of HSLA under 15N normal load. As shown, no characteristic features of severe wear are observed. Similar to the situation of AZ31B-Mg and 5182 Al alloys, no wear-regime transition occurred under the present testing condition.

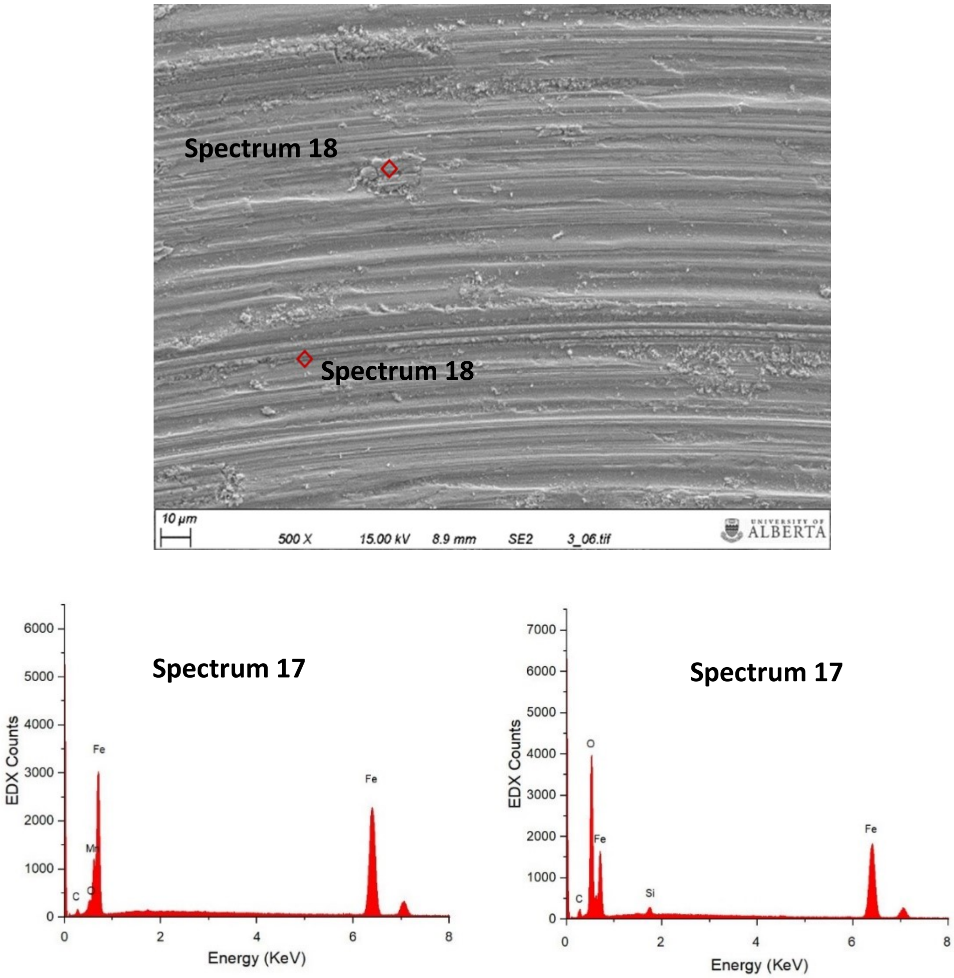

Figure 4.10 SEM and EDX microanalysis of the worn surface of HSLA under 15 N load for 18.84 m sliding distance at 1 cms^{-1} sliding speed

4.3 Friction Properties

Friction coefficients of the samples were recorded during the wear tests. Figure 4.11, figure 4.12 and figure 4.13 show the change of coefficient of friction with sliding distance for 5182 Al alloy, Mg AZ31B alloy and HSLA respectively under the normal loads of 1 N, 5 N, 10 N, 15 N for 18.84 m sliding distance at 1 cms^{-1} sliding speed. Average friction coefficients of the three alloys with errors have been shown in Fig. 4.14. As shown, average friction coefficients of the samples decreased as the contact force was increased. This could be attributed to the increase in the amount of oxide-rich wear debris and larger strain-hardening under higher loads, which increased the load-bearing capability and thus smaller real contact per unit apparent contact area, leading to lowered friction coefficient as the contact load was increased. No sign of abrupt changes in frictional behavior was observed. This implies that no wear regime transition occurred. Usually transition from mild to severe wear is associated with a sharp increase in the friction coefficient with the contact load, since a higher load breaks down the protective surface film with less difficulty and consequently increases true metallic contact [39].

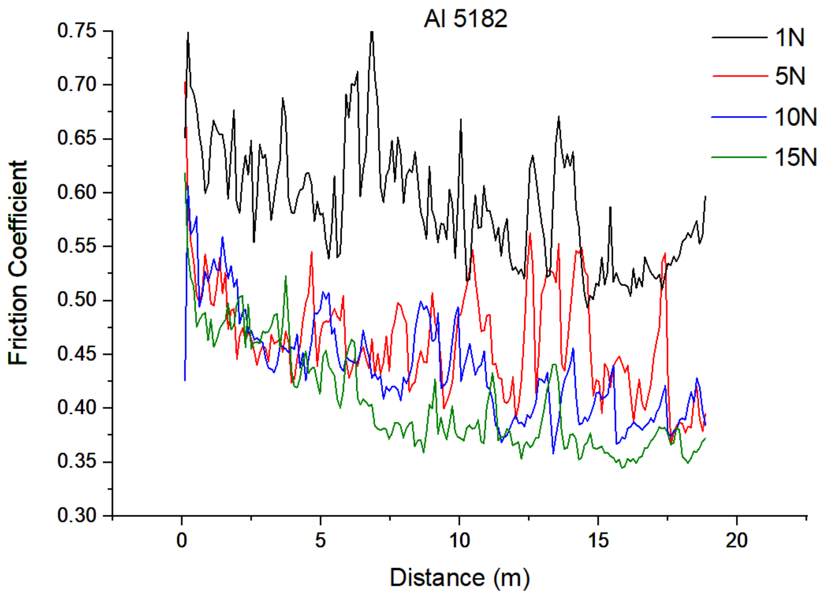

Figure 4.11 Change in the coefficient of friction versus the sliding distance for the 5182 Al alloy under the normal loads of 1 N, 5 N, 10 N, 15 N for 18.84 m sliding distance at 1 cms-1 sliding speed

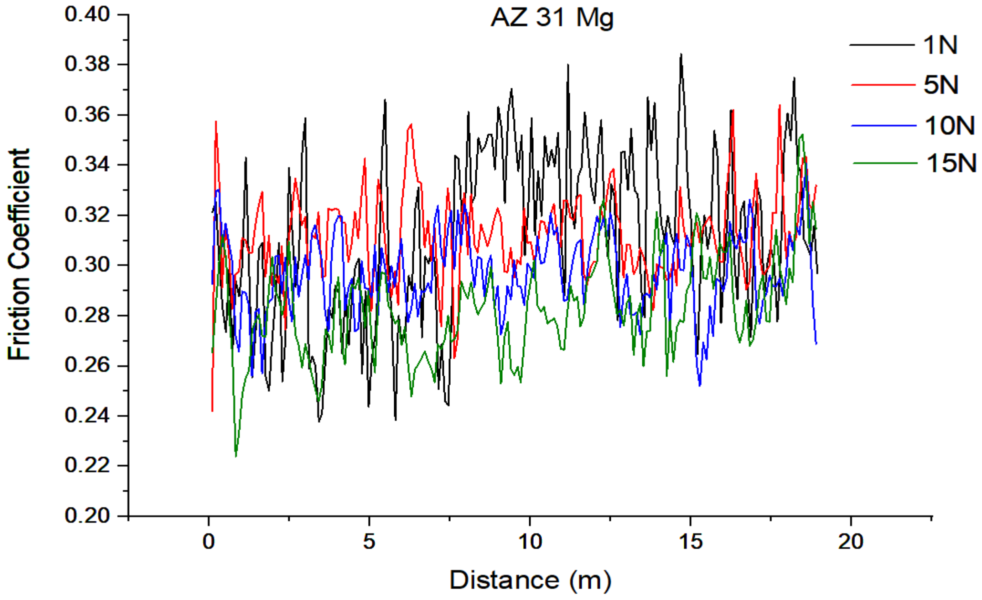

Figure 4.12 Change in the coefficient of friction versus the sliding distance for the 5182 Al alloy under the normal loads of 1 N, 5 N, 10 N, 15 N for 18.84 m sliding distance at 1 cms-1 sliding speed

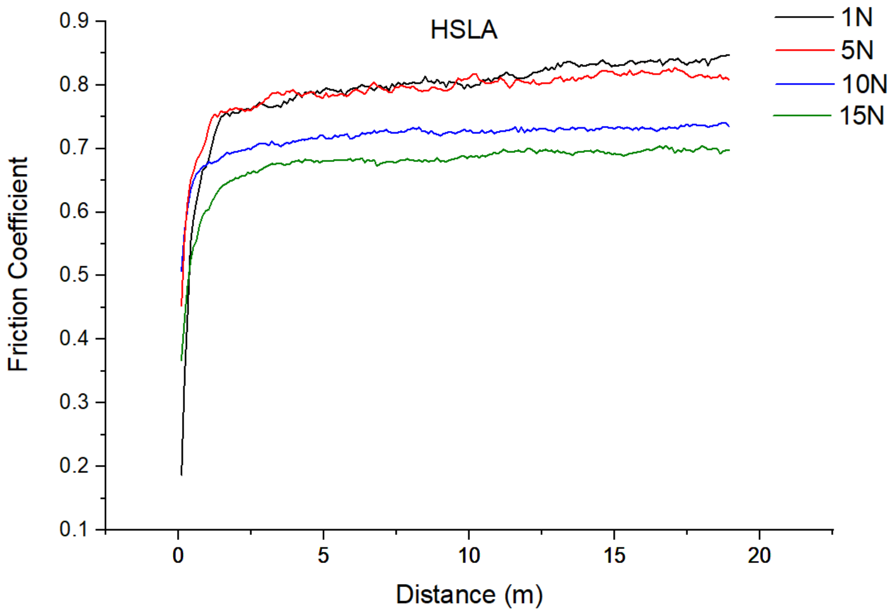

Figure 4.13 Change in the coefficient of friction versus the sliding distance for the 5182 Al alloy under the normal loads of 1 N, 5 N, 10 N, 15 N for 18.84 m sliding distance at 1 cms-1 sliding speed

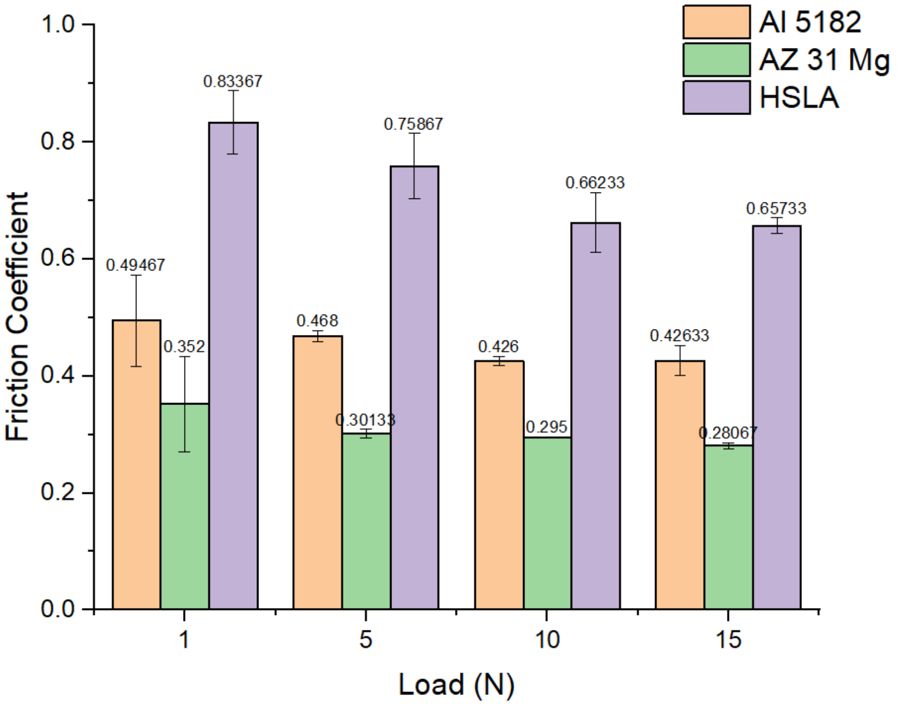

Figure 4.14 Average frictional coefficients of the three alloys with respect to the contact force..

4.4 Theoretical Consideration

During sling wear, a metallic material is abraded by asperities on the counter-face. To simplify the problem, similar to the treatment dealing with the contact geometry [39,59], we consider the wearing process involve two sub-processes, asperity indentation and plowing. Fig. 4.15 illustrates an indentation process of a single conical asperity under a normal force.

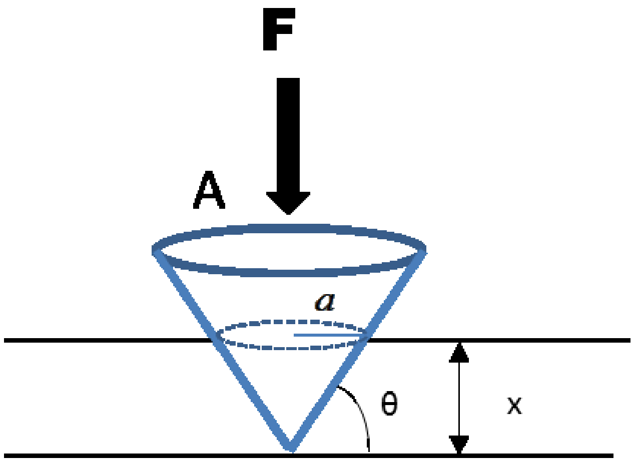

Figure 4.15 Schematic illustration of the indentation of a conical indenter on a flat surface. x is the indentation depth

Under a normal force (F), the indentation depth or penetration depth of the asperity is x and the contact area is $A = \pi a^2$, where a is the radius of the contact area and

$$\boldsymbol{x = a.\tan\theta} \tag{12}$$

The penetration depth increases as the force is increased. Fig.4.16 shows a schematic illustration of loading and unloading curves during an indentation cycle. The loading curve is represented using a general power law equation (eqn 13)

$$\boldsymbol{F = \alpha x^n} \tag{13}$$

where α and n are two fitting parameters. The value of n reflects the curvature of the loading curve, which should be related to the strain-hardening rate of the material and the indenter geometry. The value of α is related to hardness. The larger the α value, the larger is the resistance to indentation.

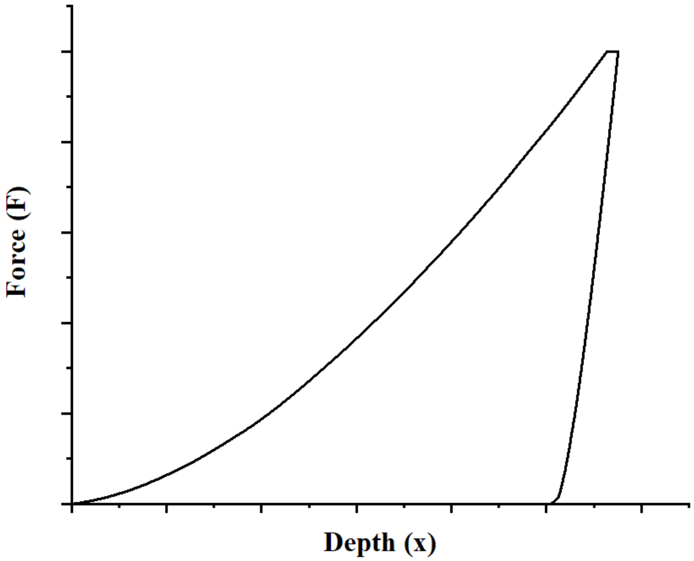

Figure 4.16 Schematic of a force-displacement diagram during the micro indentation test

From equation (13), we have $x = \left(F/\alpha\right)^{1/n}$. When the asperity with a penetration depth, x, laterally moves under a lateral wearing force, its lateral contact area with the material is

$$\boldsymbol{A_t = \frac{1}{2}(2a)x = ax = a(F/\alpha)^{\frac{1}{n}} = \left(\frac{x}{tan\theta}\right)\left(\frac{F}{\alpha}\right)^{\frac{1}{n}} = \frac{F^{2/n}}{\alpha^{2/n}tan\theta}} \tag{14}$$

When the asperity moves an infinitesimal distance, ds, the volume loss is equal to

$$\boldsymbol{dV = A_t dl = \left[\frac{F^{\frac{2}{n}}}{\alpha^{\frac{2}{n}}tan\theta}\right].ds} \tag{15}$$

Integration of this equation over a total sliding distance (S) yield

$$\boldsymbol{V = \int_0^S A_t ds = \frac{F^{\frac{2}{n}}}{\alpha^{\frac{2}{n}} tan\theta} . S = \frac{F^{\tau} S}{\alpha^{\tau} <tan\theta>}} \qquad \textbf{(16)}$$

where $\tau = 2/n$ and $1/<\tan\theta>$ is a parameter related to surface geometry or average roughness of the counter-face. According to equation (16), the volume loss (V) is proportional to F^{τ} rather than F, which deviates from that described by Archard's equation i.e. V-F relation is non-linear.

Figure 4.17 shows the indentation force (F) ~ depth (x) curves for the three alloys up to the maximum load of 500 mN. As shown, HSLA has the largest resistance to indentation, followed by the Al alloy, and AZ31B Mg alloy has the least resistance to indentation.

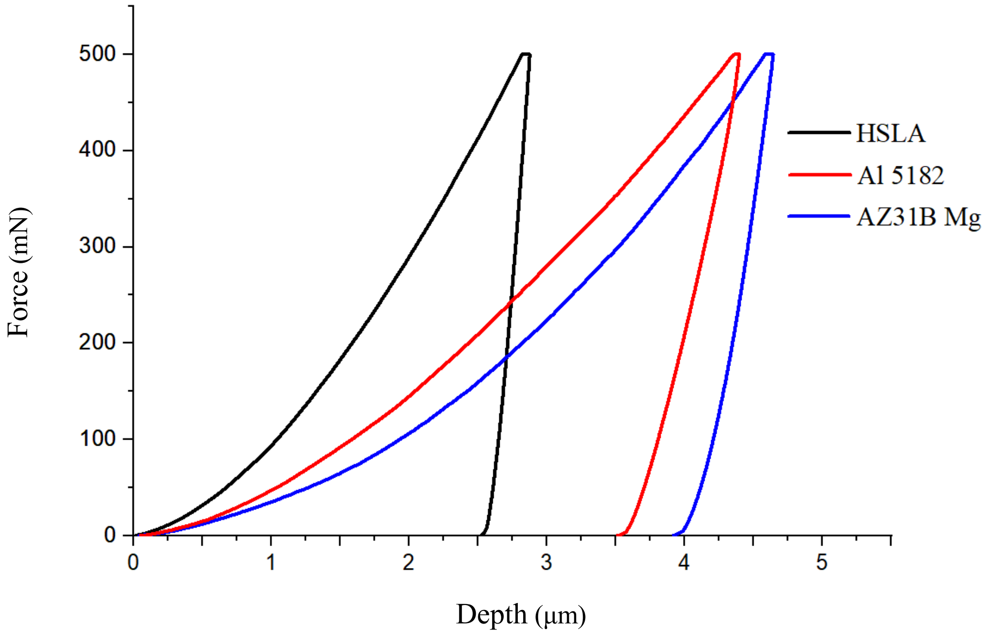

Figure 4.17 Force (F) ~ depth (x) curves of 5182 Al alloy, AZ31B Mg alloy and HSLA up to the maximum load of 500 mN.

Power law fitting of the loading portion of these three curves results in the following equations (eq. (17) to eq. (19)) of the force ~ depth relationships for the three alloys.

$$\text{HSLA: } \boldsymbol{F = 95.2\, x^{1.6}} \tag{17}$$

$$\text{Al 5182: } \boldsymbol{F = 48.7\, x^{1.58}} \tag{18}$$

$$\text{AZ31B Mg alloy: } \boldsymbol{F = 29.5\, x^{1.85}} \tag{19}$$

Comparing the equations (17), (18) and (19) with equation (13), values of α and n for the three alloys under study are given as

$\alpha = 95.2$ and $n = 1.60$ for HSLA,

$\alpha = 48.68$ and $n = 1.58$ for Al 5182,

$\alpha = 29.5$ and $n = 1.85$ for AZ31B Mg alloy.

Both α and n determine the resistance to indentation, and its variation with the indentation depth, which is reflected by the slope of F ~ d curve. The slope is expressed by

$$\boldsymbol{\frac{dF}{dx} = \alpha n x^{n-1}} \tag{20}$$

influenced by α, n and x. Fig. 4.18 illustrates F ~ x slopes of the three materials. As shown, HSLA has the highest slope, followed by Al 5182, and AZ31 has the lowest slope. The larger the slope, the larger the increase in the resistance to indentation. Such an increase in the resistance to indentation may benefit from the strain-hardening capability of the material.

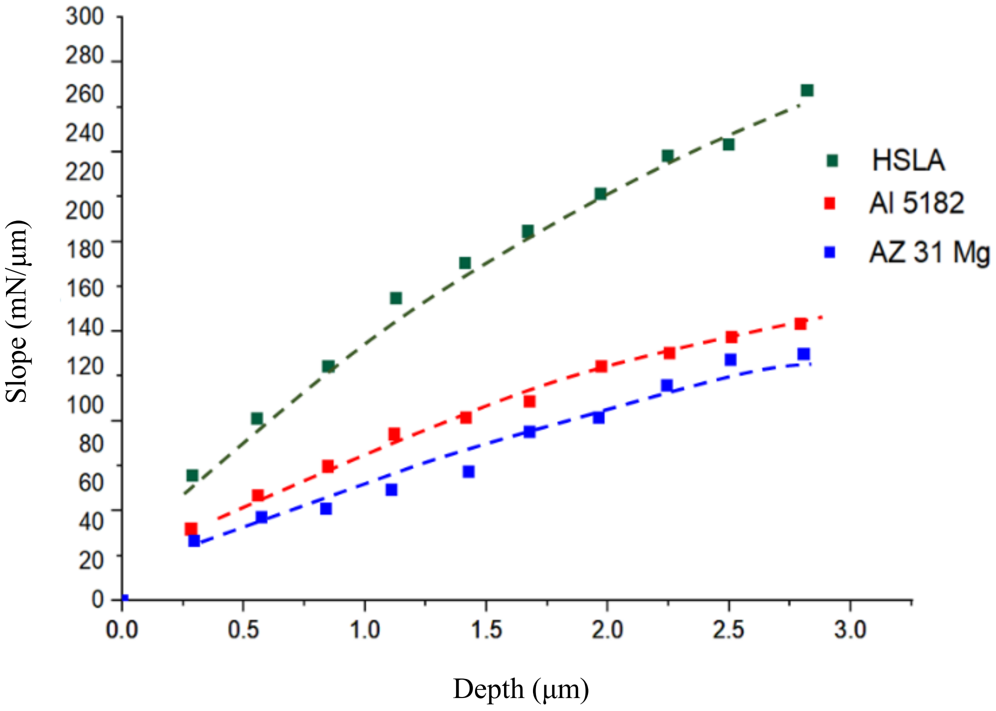

Figure 4.18 Slopes of the force~ depth curves of the three materials under study.

From figures 4.1, 4.17 and 4.18, it is clear that, the larger the α value, the higher is the wear resistance. α value is related to hardness of the target material. The effect of n on the resistance to indentation is influenced by the indentation depth. Considering the values of both α and n from eq. (17) to eq. (19), it is clear from the fig. 4.17 that, both α and n combinedly contribute to the concavity of the loading curve of indentation load ~ displacement diagram. Hosseinzadeh and Mahmoudi [60] have shown that, concavity of the loading curve is also dependent on the strain hardening exponent and yield strength of materials. Increasing both the strain hardening exponent and yield strength increases the concavity of the loading curve. Thus, it is reasonable that, both α and n are related to the strain-hardening exponent and yield strength of materials.

To simplify the analysis with focus on wear, we may directly consider the slope of volume loss ~ normal force, which is the derivative of volume loss with respect to the normal force,

$$\boldsymbol{\frac{dV}{dF} = \left(\frac{1}{\alpha^{\tau} < tan\theta >}\right) \tau F^{\tau-1}} \tag{21}$$

As indicated, the slope, *dV/dF*, is not linear with F as long as $\tau \neq 1$ and depends on both α and $\tau = 2/n$. Increasing α, which reflects higher hardness, reduces the slope. Values of $\tau = 2/n$ for the three materials measured from the indentation curves (shown in Fig.4.17) are

HSLA: $\tau = 1.25$

Al 5182: $\tau = 1.27$

AZ31: $\tau = 1.08$

Within the range of applied force for the current tests, we have

$$\frac{dV}{dF}\Big|_{HSLA} < \frac{dV}{dF}\Big|_{Al5182} < \frac{dV}{dF}\Big|_{AZ31}$$

Values of *dV/dF* of the three materials at the normal forces of 5N and 10N, respectively, are given in Table 4.1. As eq. (21) indicates, the slope is governed by both α and $\tau = 2/n$, which are determined from the indentation curve. Thus, the curvature of the indentation curve does not only provide the information on the material resistance to indentation and hardness but also that on variations in the resistance to indentation due to the strain-hardening capability. Although such variations are influenced by the indenter geometry, the strain-hardening capabilities of different materials can be ranked and compared as long as the indentation condition, including the indenter geometry, is kept the same.

4.5 Contributions of hardness and strain-hardening to the V~F curve's non-linearity

The strain-hardening capability can be evaluated based on the strain-hardening rate [61], which is the slope of true stress-strain curve, ${}^{d\sigma}\!/_{d\varepsilon}$, in the plastic deformation stage. Standard tensile tests were performed for the three alloys up to fracture.

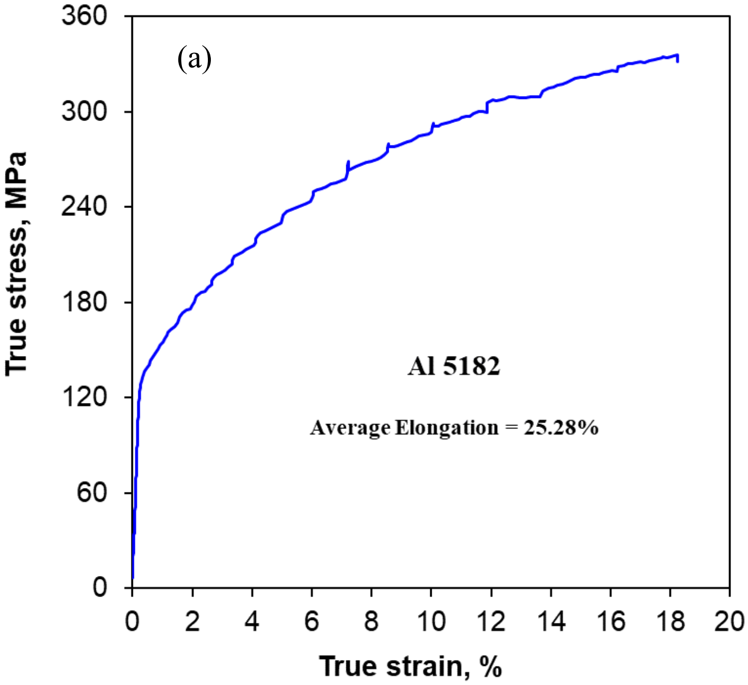

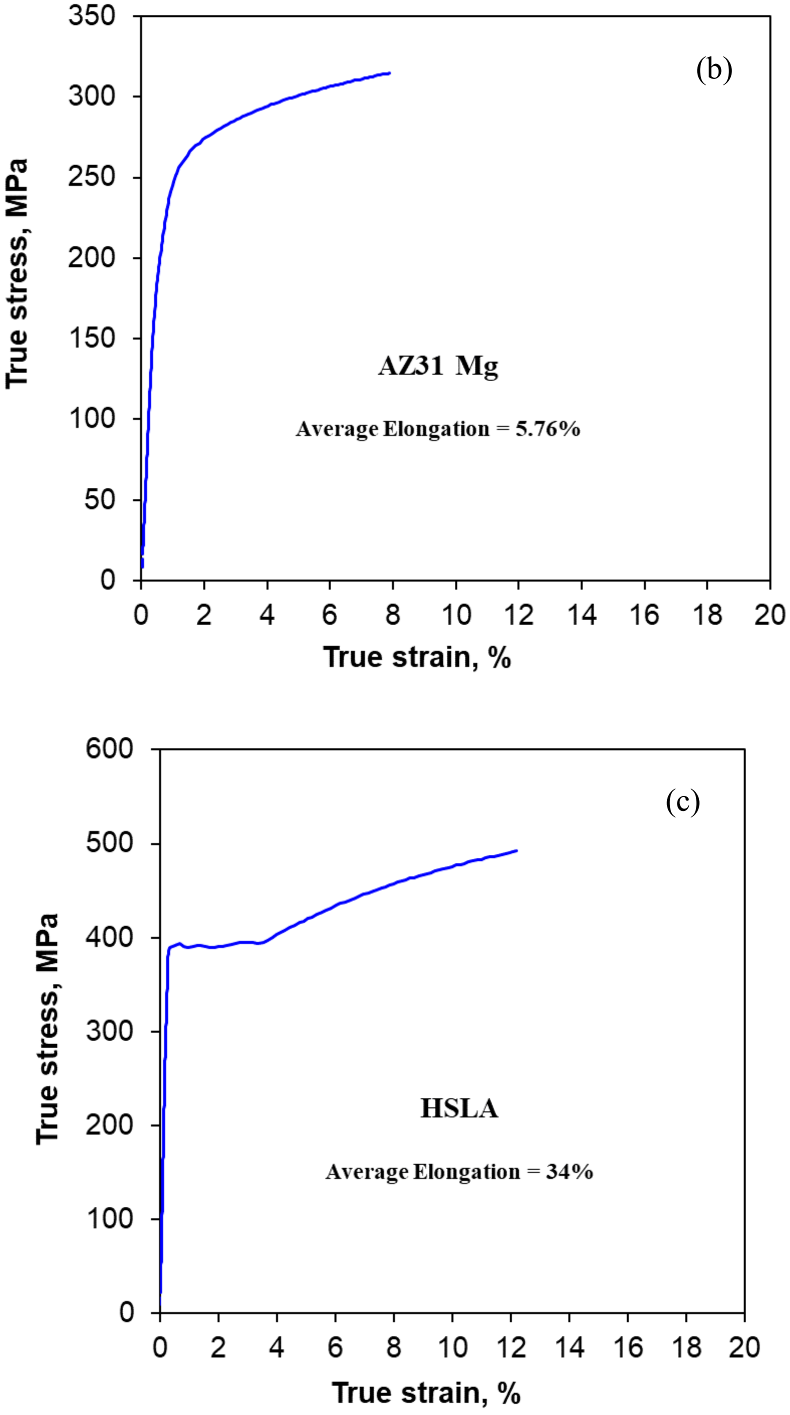

Figure 4.19 Representative stress-strain curves of (a) AZ31, (b) Al5182, and (c) HSLA.

Fig. 4.19 illustrates representative stress-strain curves of Al5182 (fig. 4.19a), AZ31 (fig. 4.19b) and HSLA (fig. 4.19c) alloys, based on which the average slopes of the three materials were estimated. They are 4.8 MPa, 9.4 MPa, and 11.5 MPa, respectively, indicating that, to generate the same strain increment, the required increment of stress is the least for AZ31 and the largest for HSLA. Besides, the stress-strain slope varies with the stress, which also influences the curvature of the volume loss (V) ~ force (F) curve i.e. contributes to the non-linear relationship between the volume loss and the normal force. Eq. (21) indicates that the slope, ${dV}/{dF}$, related to the curvature of $V \sim F$ curve, is dependent on the strain-hardening, hardness and the normal force, influenced by the values of α and τ as well as F.

The plastic portion of these stress strain curves is generally represented by the eq. (11),

$$\boldsymbol{\sigma = K_s \varepsilon^m}$$

where m represents the strain hardening exponent. Allometric fittings of the plastic portion of the stress ~ strain curves give the following strain hardening exponent values,

For Al 5182, $m = 0.26$, $k_s = 156.7$ MPa

For HSLA, $m = 0.18$, $k_s = 314.6$ MPa

For AZ 31, $m = 0.105$, $k_s = 254.2$ MPa

As shown, m (Al5182) > m (HSLA) > m (AZ31), and k_s (HSLA) > k_s (AZ31) > k_s (Al5182), implying that the increase in hardness of Al 5182 is the largest and that of AZ31 is the smallest. Such orders of m and k_s are different from those of τ or n and α determined from the indentation curves. This implies that the effect of the variation in mechanical strength due to strain-hardening on wear is a combined effect of n and α or m and k_s.

Assuming the samples have the same surface geometry or roughness on average, we may compare their slopes of measured V ~ F curves.

$$\left(\frac{dV}{dF}\right)_{HSLA} : \left(\frac{dV}{dF}\right)_{Al5182} : \left(\frac{dV}{dF}\right)_{AZ31B\ Mg} =$$

$$\left(\frac{\tau F^{\tau-1}}{\alpha^{\tau}}\right)_{HSLA} : \left(\frac{\tau F^{\tau-1}}{\alpha^{\tau}}\right)_{Al5182} : \left(\frac{\tau F^{\tau-1}}{\alpha^{\tau}}\right)_{AZ31B\ Mg} \tag{22}$$

The ratios of $(\frac{dV}{dF})_{HSLA} : (\frac{dV}{dF})_{Al5182} : (\frac{dV}{dF})_{AZ31B\ Mg}$ for two loads, 5N and 10N, were calculated and presented in Table 4.1. Experimentally measured ratios are also given for comparison. As shown, the calculated and measured values are consistent, implying that the model can reasonably describe the observed phenomena.

Table 4.1 Experimentally determined parameters of HSLA, Al5182 and AZ31

Alloy	τ	α	m	k_s (mpa)	F (N)	$\frac{dV}{dF}(\overline{\tan\theta}) = \frac{\tau F^{\tau-1}}{\alpha^{\tau}}$ $(\times 10^{-3})$	$\left(\frac{dV}{dF}\right)_{HSLA} : \left(\frac{dV}{dF}\right)_{Al5182} : \left(\frac{dV}{dF}\right)_{AZ31}$
HSLA	1.25	95.2	0.18	314.6	5	6.3	Calculated:
					10	7.5	5N: $\left(\frac{dv}{dF}\right)_{HSLA,5N} : \left(\frac{dv}{dF}\right)_{Al5182,5N} : \left(\frac{dv}{dF}\right)_{AZ31,5N} = 1:2.3:5.0$
Al5182	1.27	48.7	0.26	156.7	5	14.3	10N: $\left(\frac{dv}{dF}\right)_{HSLA,10N} : \left(\frac{dv}{dF}\right)_{Al5182,10N} : \left(\frac{dv}{dF}\right)_{AZ31,10N} = 1:2.3:4.5$
					10	17.1	Experimental:
AZ31	1.08	29.5	0.105	254.2	5	31.8	5N: $\left(\frac{dv}{dF}\right)_{HSLA,5N} : \left(\frac{dv}{dF}\right)_{Al5182,5N} : \left(\frac{dv}{dF}\right)_{AZ31,5N} = 1:3.8:7.9$
					10	33.6	10N: $\left(\frac{dv}{dF}\right)_{HSLA,10N} : \left(\frac{dv}{dF}\right)_{Al5182,10N} : \left(\frac{dv}{dF}\right)_{AZ31,10N} = 1:3.5:4.2$

According to the information provided in Table 4.1, the ratio of slopes of V~F curves for the three materials predicted with the proposed model with equation (21) are consistent with experimentally measured values. The slope is dependent on α and τ , which are related to hardness and strain-hardening capability.

The non-linearity of *V~F* curve can be estimated from the indentation curve, which is a measure of the resistance to indentation and also reflects the resistance to penetration of counter-face's asperities. From the indentation load-depth curve as those illustrated in Fig. 4.17, one may determine α and τ of a material. The non-linearity of V~F curve and the dependence of the volume loss on the normal force can thus be estimated by eq. (22)

$$\boldsymbol{V = \frac{F^{\tau}.S}{\alpha^{\tau}}\left(\frac{1}{\overline{\overline{tan\theta}}}\right)} \tag{22}$$

On the other hand, from the non-linearity of V ~ F curve, one may also determine α and τ , and thus obtain relevant information on variations in material properties during the wearing process.

4.6 Remarks

The non-linear relation between wear loss and contact force is ascribed to the variation in mechanical strength during the wear process, which is related to the strain-hardening capability. Such strengthening capability can be linked to the indentation behavior or the strain hardening rate deferential from the tensile test.

4.7 Limitations and Applicability of the Model:

a) The model presented in this study is limited to materials subjected to relatively low contact load and sliding speed, with which no wear-regime (from mild to severe wear) transition occur.

b) This proposed model is applicable to wear caused by contact loads at low strain rates, since it relates the quasi-static indentation testing to sliding wear condition, which is a dynamic process. However, if high-velocity indentation behavior of materials is possibly determined, the model is still applicable for linking the indentation behavior with the wear resistance of materials under wear attacks at higher sliding velocities.

c) This model is also applicable for the wear behavior of cold-worked materials, which have lower strain-hardeninig rates due to prior plastic deformation.

Chapter 5 Conclusion and Future Research

5.1 Conclusion

Archard's equation is widely used to estimate the wear resistance of materials based on hardness, which shows a linear relationship between the material loss and the applied normal force. However, it is often observed that the material loss increases nonlinearly with the normal force. The present study is conducted to have a further look at the non-linear relationship and correlate it to variations in hardness and strain-hardening effect. A relevant model is proposed, which shows that the volume loss (*V*) is not linear to *F*. The following main conclusions are drawn.

1) The degree of non-linearity depends on both hardness and the strain hardening behavior of the material, which can be reflected by its indentation vs depth curve, $F = \alpha \cdot x^n$. Values of the coefficients, α and n, can be obtained from the power law fitting of the loading portion of the indentation curve.
2) *dV/dF* is influenced by both the hardness (reflected by α) and the strain-hardening exponent (represented by $\tau = 2/n$). Increases in both of these coefficients decrease *dV/dF*.
3) The proposed model links the material loss-force curve with the indentation behavior, from which more information on material properties and variations in the material behavior during the wearing process could be extracted.

5.2 Future Research Opportunities:

Several future research opportunities have been listed below –

1. Establish relation between the strain hardening rate or $\boldsymbol{\sigma = K_s \varepsilon^m}$ and the indentation behavior, i.e. $\boldsymbol{F = \alpha x^n}$, so that one can relate the non-linear wear vs force relationship to commonly used parameters that characterize the strain hardening capability
2. Investigate how the crystal structure and associated slip systems affect non-linear relation between wear loss and the contact force.
3. Since cold worked materials are used in industry, it would be worth investigating how the cold-work affect the non-linear relation between volume loss and force.
4. Second-phase strengthening is a common approach to strengthen materials. It would be worth investigating effect of second phases on the non-linear relation between volume loss and force.

Bibliography

1. Kloss, H. & Wäsche, R. Analytical approach for wear prediction of metallic and ceramic materials in tribological applications. *Wear* **266,** 476–481 (2009).

2. Holmberg, K. & Erdemir, A. Influence of tribology on global energy consumption, costs and emissions. *Friction* **5,** 263–284 (2017).

3. Lim, S. C. & Ashby, M. F. Overview no. 55 wear-mechanism maps. *Acta Metall.* **35,** 1–24 (1987).

4. Ludema, K. C. *Friction, wear, lubrication: a textbook in tribology*. (CRC press, 1996).

5. Meng, H. C. & Ludema, K. C. Wear models and predictive equations: their form and content. *Wear* **181–183,** 443–457 (1995).

6. Gotsmann, B. & Lantz, M. A. Atomistic wear in a single asperity sliding contact. *Phys. Rev. Lett.* **101,** (2008).

7. Archard, J. F. Contact and rubbing of flat surfaces. *J. Appl. Phys.* **24,** 981–988 (1953).

8. ASTM. ASTM G40 - Standard Terminology Relating to Wear and Erosion. *ASTM* 9 (2017). doi:10.1520/G0040-17

9. Glaeser, W. A. Friction and Wear. *IEEE Trans. Parts, Hybrids, Packag.* **7,** 99–105 (1971).

10. Raymond, G. B. *Mechanical wear fundamentals and testing*. *Marcel Dekker Inc.,*

USA (2004). doi:doi:10.1201/9780203021798.fmatt

11. Hogmark, S., Jacobson, S. & Vingsbo, O. Surface Damage. in *ASM Handbook, Volume 18: Friction, Lubrication, and Wear Technology* (1992).
12. Varenberg, M. Towards a unified classification of wear. *Friction* **1,** 333–340 (2013).
13. Kato, K. Classification of wear mechanisms/models. *Proc. Inst. Mech. Eng. Part J J. Eng. Tribol.* **216,** 349–355 (2002).
14. Yamamoto, T. & Buckley, D. H. Wear mechanism based on adhesion. (1982).
15. Kato, K. Abrasive wear of metals. *Tribol. Int.* **30,** 333–338 (1997).
16. Kapoor, A. & Johnson, K. L. Plastic ratchetting as a mechanism of metallic wear. *Proc. R. Soc. Lond. A* **445,** 367–384 (1994).
17. Bowden, F. P., Tabor, D. & Palmer, F. The Friction and Lubrication of Solids. *Am. J. Phys.* **19,** 428–429 (1951).
18. Burwell, J. T. & Strang, C. D. On the empirical law of adhesive wear. *J. Appl. Phys.* **23,** 18–28 (1952).
19. Archard, J. F. & Hirst, W. The Wear of Metals under Unlubricated Conditions. *Proc. R. Soc. A Math. Phys. Eng. Sci.* **236,** 397–410 (1956).
20. Hokkirigawa, K., Kato, K. & Li, Z. Z. The effect of hardness on the transition of the abrasive wear mechanism of steels. *Wear* **123,** 241–251 (1988).
21. Murray, M. J., Mutton, P. J. & Watson, J. D. Abrasive wear mechanisms in steels.

J. Lubr. Technol. **104,** 9–16 (1982).

22. Fang, L., Zhou, Q. D. & Li, Y. J. An explanation of the relation between wear and material hardness in three-body abrasion. *Wear* **151,** 313–321 (1991).

23. Kluge, A., Langguth, K., Öchsner, R., Kobs, K. & Ryssel, H. Examination of wear, hardness and friction of nitrogen-, boron-, carbon-, silver-, lead- and tin-implanted steels with different chromium contents. *Mater. Sci. Eng. A* **115,** 261–265 (1989).

24. Krause, H. & Tackenberg, W. The influence of hardness difference on the frictional and wear behaviour of steel/copper alloy pairs in plane sliding friction under mixed friction conditions. *Wear* **64,** 291–302 (1980).

25. Xuan, J. L., Hong, I. T. & Fitch, E. C. Hardness effect on three-body abrasive wear under fluid film lubrication. *J. Tribol.* **111,** 35–40 (1989).

26. Atkins, A. G. Slice–push, formation of grooves and the scale effect in cutting. *Interface Focus* **6,** 20160019 (2016).

27. Li, D. Y. Abrasive Wear. in *ASM Handbook, Volume 18: Friction, Lubrication, and Wear Technology* (ed. Totten, G. E.) (2017).

28. Glaeser, W. *Materials for tribology*. **20,** (Elsevier, 1992).

29. Liu, R. & Li, D. Y. Modification of Archard's equation by taking account of elastic/pseudoelastic properties of materials. *Wear* **251,** 956–964 (2001).

30. Wayman, C. M. *Introduction to the crystallography of martensitic transformations*. (Macmillan, 1964).

31. Otsuka, K. & Shimizu, K. Pseudoelasticity and shape memory effects in alloys. *Int. Met. Rev.* **31,** 93–114 (1986).

32. Doerner, M. F. & Nix, W. D. A method for interpreting the data from depth-sensing indentation instruments. *J. Mater. Res.* **1,** 601–609 (1986).

33. Torrance, A. A. The correlation of abrasive wear tests. *Wear* **63,** 359–370 (1980).

34. Yi-Ling, W. & Zi-Shan, W. An analysis of the influence of plastic indentation on three-body abrasive wear of metals. *Wear* **122,** 123–133 (1988).

35. Pintaude, G. Introduction of the Ratio of the Hardness to the Reduced Elastic Modulus for Abrasion. in *Tribology - Fundamentals and Advancements* (2013). doi:10.5772/55470

36. Stilwell, N. A. & Tabor, D. Elastic recovery of conical indentations. *Proc. Phys. Soc.* **78,** 169–179 (1961).

37. Ceschini, L., Martini, C. & Morri, A. Dry sliding wear of an induction-hardened, high-silicon medium-carbon microalloyed steel. *Tribol. Int.* **92,** 493–502 (2015).

38. Zhang, J. & Alpas, A. T. Transition between mild and severe wear in aluminium alloys. *Acta Mater.* **45,** 513–528 (1997).

39. Hutchings, I. & Shipway, P. *Tribology: Friction and wear of engineering materials: Second Edition*. *Tribology: Friction and Wear of Engineering Materials: Second Edition* (2017).

40. Glascott, J., Stott, F. H. & Wood, G. C. The effectiveness of oxides in reducing sliding wear of alloys. *Oxid. Met.* **24,** 99–114 (1985).

41. Vuong, T. T. *et al.* Investigation of a transitional wear model for wear and wear-type rail corrugation prediction. *Wear* **271,** 287–298 (2011).

42. Lewis, R. & Olofsson, U. Mapping rail wear regimes and transitions. *Wear* **257,** 721–729 (2004).

43. Lim, S. C. & Ashby, M. F. Overview no. 55 Wear-Mechanism maps. *Acta Metall.* **35,** 1–24 (1987).

44. Chen, H. & Alpas, A. T. Sliding wear map for the magnesium alloy Mg-9Al-0.9 Zn (AZ91). *Wear* **246,** 106–116 (2000).

45. Wang, Z. . *et al.* Effect of surface nanocrystallization on friction and wear properties in low carbon steel. *Mater. Sci. Eng. A* **352,** 144–149 (2003).

46. Elmadagli, M. & Alpas, A. T. Progression of wear in the mild wear regime of an Al-18.5% Si (A390) alloy. *Wear* **261,** 367–381 (2006).

47. Liang, C., Han, X., Su, T. F., Lv, X. X. & An, J. Roles of Friction-Induced Strain Hardening and Recrystallization in Dry Sliding Wear of AZ31 Magnesium Alloy. *Trans. Indian Inst. Met.* **68,** 89–98 (2014).

48. William, F. H. & Hosford, H. Mechanical behavior of materials. *USA Univ. Michigan. Google Sch.* (2005).

49. Cheng, Y. T. & Cheng, C. M. Scaling approach to conical indentation in elastic-plastic solids with work hardening. *J. Appl. Phys.* **84,** 1284–1291 (1998).

50. Callister, W. & Rethwisch, D. *Materials science and engineering: an introduction. Materials Science and Engineering* **94,** (2007).

51. Van Phan, T. Grain scale simulation of local deformation behavior. *Asia Pacific J. Comput. Eng.* **1,** 10 (2014).

52. Van Vliet, K. J. 3.032 Mechanical behavior of materials. *Massachusetts Inst. Technol. Cambridge, MA* (2006).

53. Poerschke, D. The Effects of forging on the microstructure and tensile properties of magnesium alloys AZ31 and ZK60. *Case West. Reserv. Univ. Cleveland, OH, USA* (2009).

54. ASTM. ASTM G99-17: Standard Test Method for Wear Testing with a Pin-on-Disk Apparatus. *ASTM Int.* **G99,** (2017).

55. Tribology used to Compare Rotative Wear and Linear Wear. (2017). Available at: https://www.azonano.com/article.aspx?ArticleID=4708.

56. Optical Profiler Basics. Available at: https://www.zygo.com/?/met/profilers/opticalprofilersabout.htm.

57. Klaus Freischlad. OPTICAL SURFACE PROFILING: Profilometer advances benefit surface analysis, film-thickness measurement. (2010). Available at: https://www.laserfocusworld.com/articles/print/volume-46/issue-1/features/optical-surface-profiling.html.

58. Niu, X. D. *et al.* Effects of Loading and Sliding Speed on the Dry Sliding Wear Behavior of Mg-3Al-0.4Si Magnesium Alloy. *Tribol. Trans.* **60,** 238–248 (2017).

59. Ernest, R. Friction and wear of materials. *John Willey Sons, Inc. New York* 44–238 (1995).

60. Hosseinzadeh, A. R. & Mahmoudi, A. H. Determination of mechanical properties using sharp macro-indentation method and genetic algorithm. *Mech. Mater.* **114,** 57–68 (2017).

61. Afrin, N., Chen, D. L., Cao, X. & Jahazi, M. Strain hardening behavior of a friction stir welded magnesium alloy. *Scr. Mater.* **57,** 1004–1007 (2007).

Appendix A

This appendix presents the images of the loading curve of the indentation Load (F) ~ Depth (*x*) diagram with allometric fitting for Al-5182 alloy, AZ31B Mg alloy and HSLA

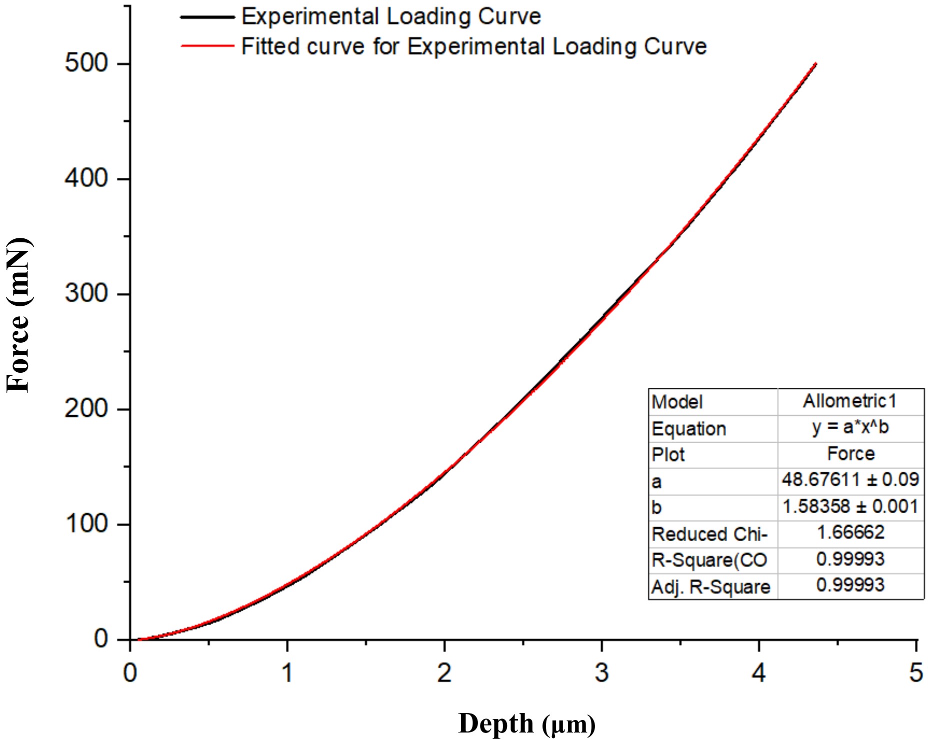

Figure A.1 Allometric fitting to the Indentation Force (F) ~ depth (x) curve for the loading portion of 5182 Al alloy up to the maximum load of 500 mN

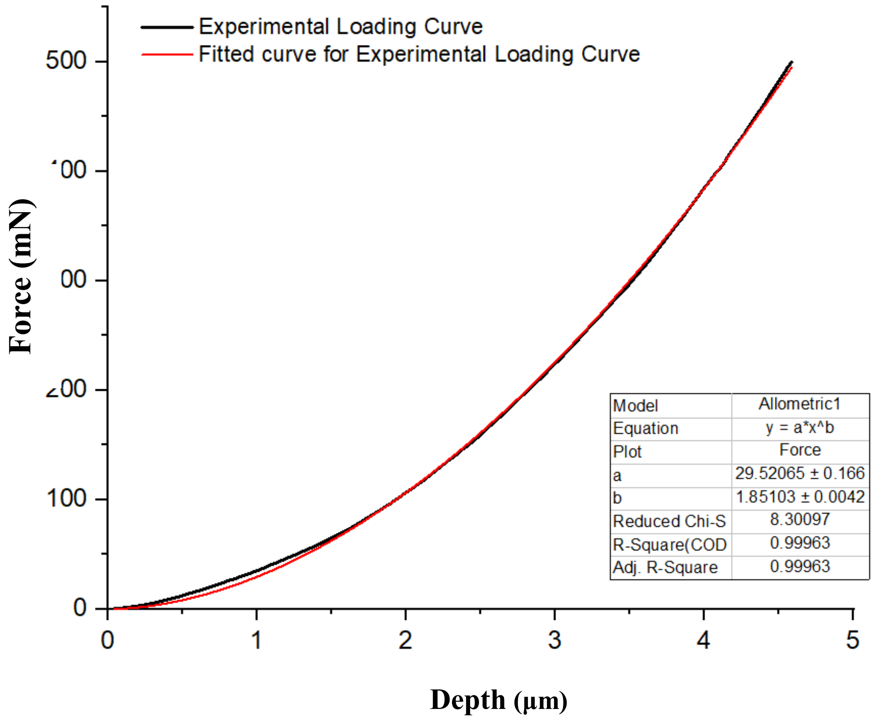

Figure A.2 Allometric fitting to the Indentation Force (F) ~ depth (x) curve for the loading portion of AZ31B Mg alloy up to the maximum load of 500 mN

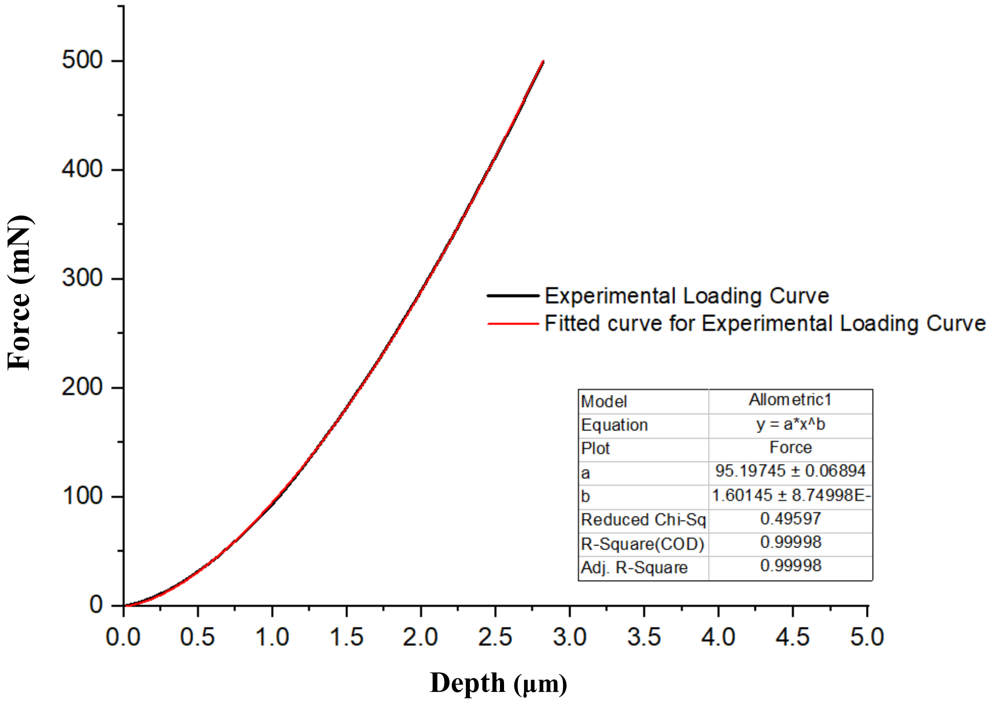

Figure A.3 Allometric fitting to the Indentation Force (F) ~ depth (x) curve for the loading portion of HSLA up to the maximum load of 500 mN

Appendix B

This appendix presents the images of the Plastic portion of True stress ~ True strain diagram from tensile test with allometric fitting for Al-5182 alloy, AZ31B Mg alloy and HSLA

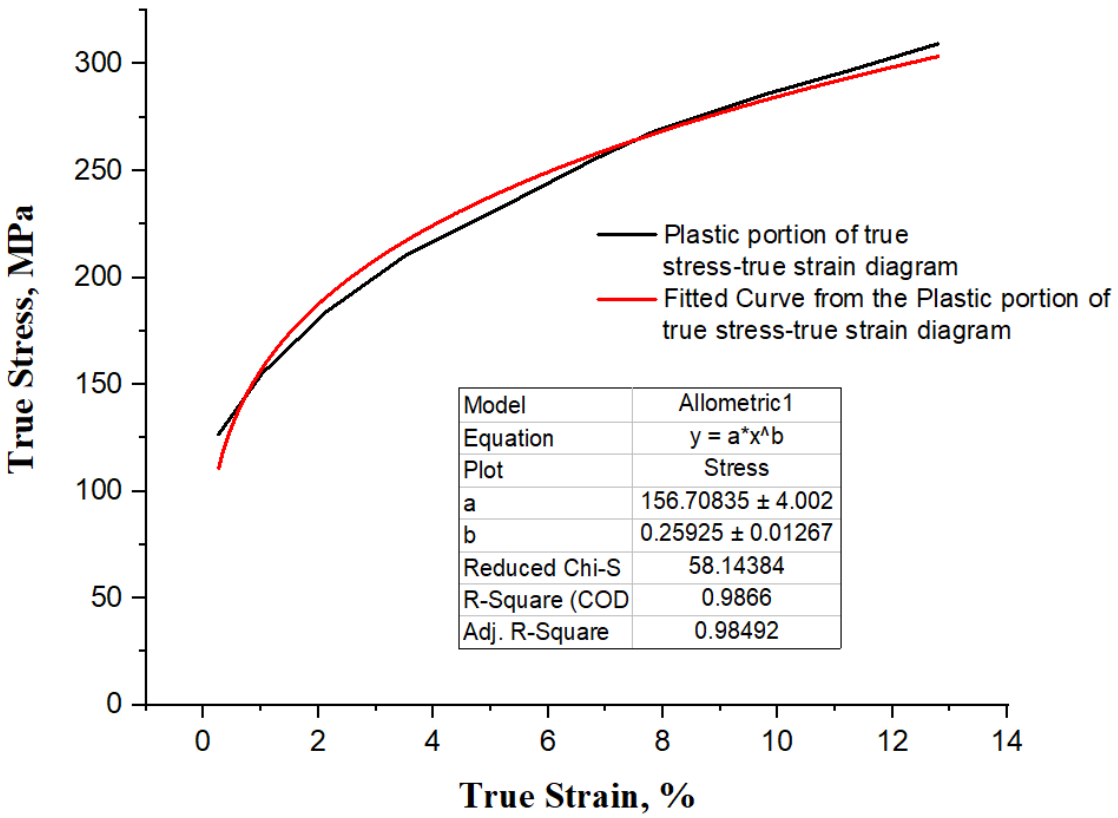

Model	Allometric1
Equation	y = a*x^b
Plot	Stress
a	156.70835 ± 4.002
b	0.25925 ± 0.01267
Reduced Chi-S	58.14384
R-Square (COD	0.9866
Adj. R-Square	0.98492

Figure B.1 Allometric fitting to the plastic deformation portion of the true stress- true strain curves for Al 5182 alloy

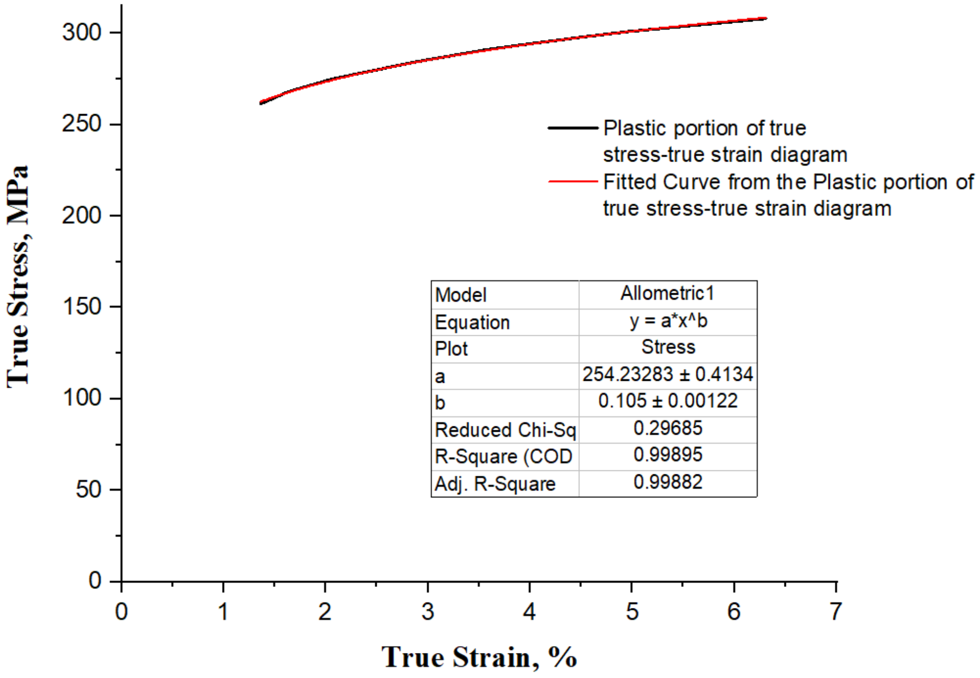

Model	Allometric1
Equation	y = a*x^b
Plot	Stress
a	254.23283 ± 0.4134
b	0.105 ± 0.00122
Reduced Chi-Sq	0.29685
R-Square (COD	0.99895
Adj. R-Square	0.99882

Figure B.2 Allometric fitting to the plastic deformation portion of the true stress- true strain curves for AZ31B-Mg alloy

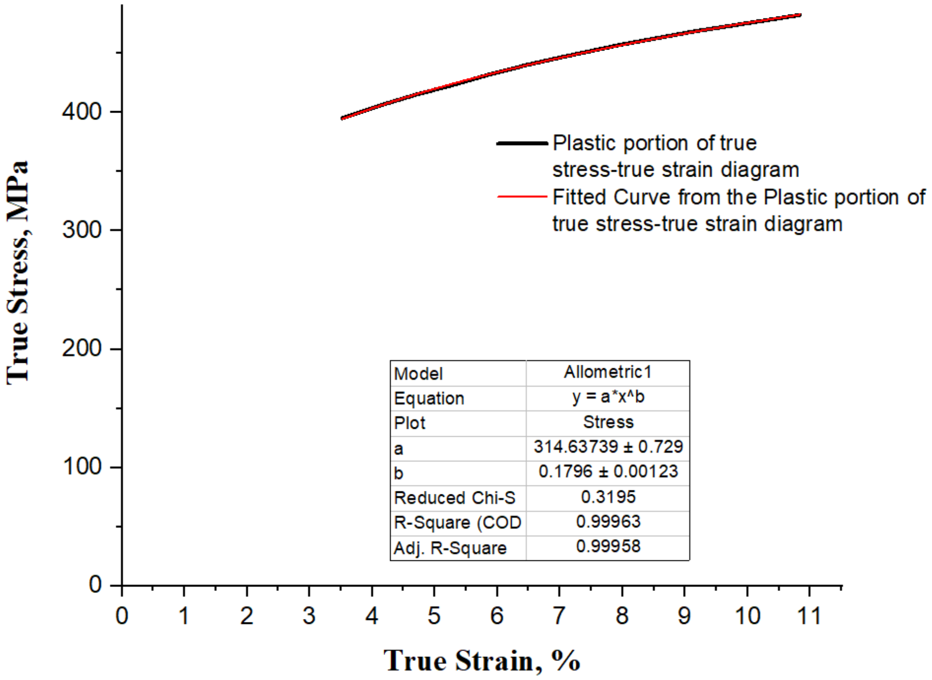

Model	Allometric1
Equation	y = a*x^b
Plot	Stress
a	314.63739 ± 0.729
b	0.1796 ± 0.00123
Reduced Chi-S	0.3195
R-Square (COD	0.99963
Adj. R-Square	0.99958

Figure B.3 Allometric fitting to the plastic deformation portion of the true stress- true strain curves for HSLA

Appendix C

This appendix presents the images of the volume loss vs force diagrams for Al-5182 alloy, AZ31B Mg alloy and HSLA showing the *dV/dF* slopes at 5N and 10N loads.

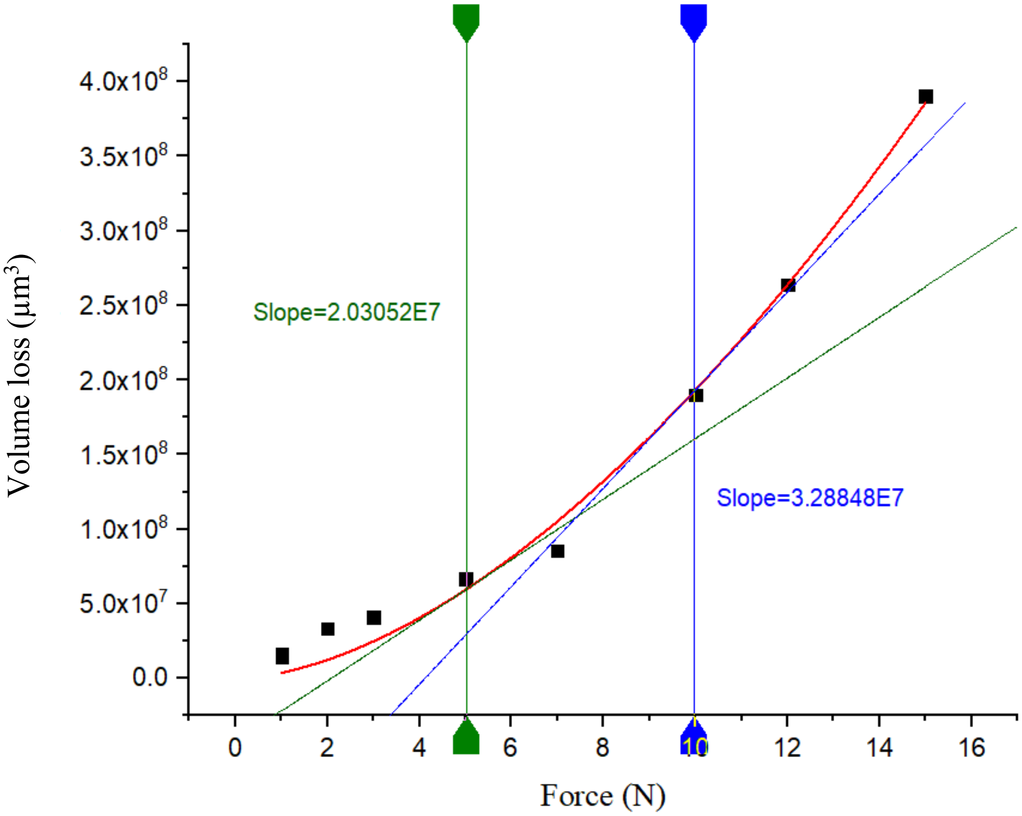

Figure C.1 Volume loss (μm^3) vs Force (N) diagram for Al 5182 alloy showing dV/dF slopes at 5N and 10 N loads

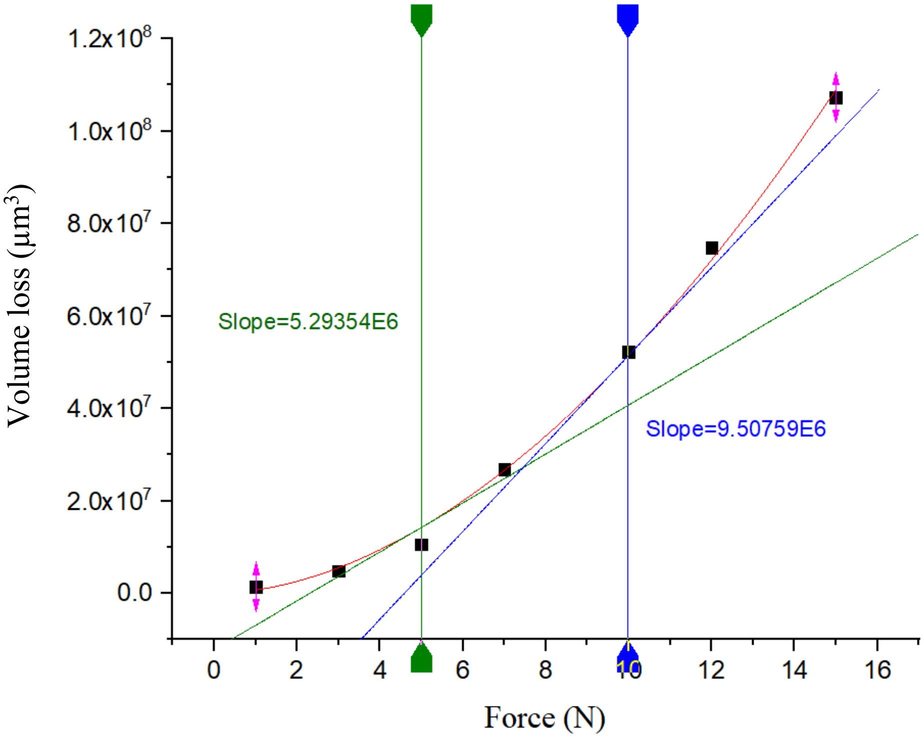

Figure C.2 Volume loss (μm^3) vs Force (N) diagram for HSLA showing dV/dF slopes at 5N and 10 N loads

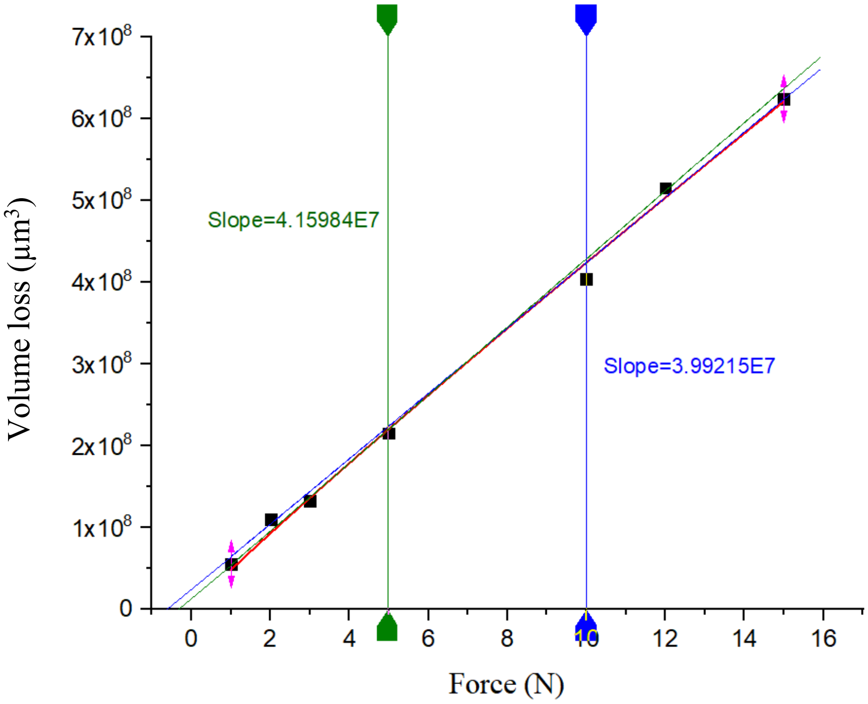

Figure C.3 Volume loss (μm^3) vs Force (N) diagram for AZ31B-Mg alloy showing dV/dF slopes at 5N and 10 N loads